

Superconducting and normal-state properties of APd_2As_2 ($A = Ca, Sr, Ba$) single crystals

V. K. Anand,^{*} H. Kim, M. A. Tanatar, R. Prozorov, and D. C. Johnston[†]

Ames Laboratory and Department of Physics and Astronomy, Iowa State University, Ames, Iowa 50011, USA

(Received 26 April 2013; revised manuscript received 29 May 2013; published 20 June 2013)

The synthesis and crystallography, magnetic susceptibility χ , magnetization M , specific heat C_p , in-plane electrical resistivity ρ , and in-plane magnetic penetration depth measurements are reported for single crystals of APd_2As_2 ($A = Ca, Sr, Ba$) versus temperature T and magnetic field H . The crystals were grown using PdAs self-flux. $CaPd_2As_2$ and $SrPd_2As_2$ crystallize in a collapsed body-centered tetragonal $ThCr_2Si_2$ -type structure ($I4/mmm$), whereas $BaPd_2As_2$ crystallizes in the primitive tetragonal $CeMg_2Si_2$ -type structure ($P4/mmm$), in agreement with literature data. The $\rho(T)$ data exhibit metallic behavior for all three compounds. Bulk superconductivity is reported for $CaPd_2As_2$ and $SrPd_2As_2$ below $T_c = 1.27$ and 0.92 K, respectively, whereas only a trace of superconductivity is found in $BaPd_2As_2$. No other phase transitions were observed. The $\chi(T)$ and $M(H)$ data reveal anisotropic diamagnetism in the normal state, with $\chi_c > \chi_{ab}$ for $CaPd_2As_2$ and $BaPd_2As_2$, and $\chi_c < \chi_{ab}$ for $SrPd_2As_2$. The normal and superconducting state data indicate that $CaPd_2As_2$ and $SrPd_2As_2$ are conventional type-II nodeless s -wave electron-phonon superconductors. The electronic superconducting state heat capacity data for $CaPd_2As_2$, which has an extremely sharp heat capacity jump at T_c , are analyzed using our recent elaboration of the α -model of the BCS theory of superconductivity, which indicates that the s -wave gap in this compound is anisotropic in momentum space.

DOI: [10.1103/PhysRevB.87.224510](https://doi.org/10.1103/PhysRevB.87.224510)

PACS number(s): 74.70.Xa, 74.25.Bt, 74.25.Op, 74.25.N–

I. INTRODUCTION

The observation of high-temperature superconductivity (SC) with transition temperatures $T_c \lesssim 38$ K in doped 122-type iron arsenides such as in $A_{1-x}K_xFe_2As_2$ ($A = Ba, Sr, Ca$, and Eu) compounds has stimulated great interest in these materials.^{1–15} The parent compounds AFe_2As_2 with $A = Ca, Sr$, and Ba are itinerant antiferromagnetic (AF) semimetals that undergo a structural distortion from a tetragonal structure to an orthorhombic one on cooling below room temperature. On cooling, the structural transition is coincident with or precedes a long-range AF itinerant spin density wave (SDW) transition. Superconductivity in these compounds emerges upon suppression of the SDW transition that can be achieved either by partial chemical substitutions at either the A , Fe , or As sites or by application of external pressure.¹¹ The same phenomenology is found in the high- T_c cuprates where the long-range AF order must be largely suppressed by doping prior to the emergence of superconductivity, but strong dynamic AF spin fluctuations must still be present. Thus, the iron arsenides and the high- T_c cuprates have a similar generic phase diagram for the emergence of superconductivity, even though the cuprate parent compounds are AF insulators rather than SDW semimetals.^{11–13,16–18}

The partial substitutions at the Fe -site in AFe_2As_2 by transition metals M in $Ba(Fe_{1-x}M_x)_2As_2$ with $M = Cr, Mn, Co, Ni, Cu, Ru, Rh$, and Pd have recently been studied both theoretically and experimentally from the perspective of the degree of charge doping because of the changes in the magnetic and SC properties caused by such substitutions.^{6,12,19–39} The substitutions for the Fe atoms by the $3d$ elements Co and Ni and the $4d$ elements Rh and Pd which have higher numbers of outer-shell d electrons than that of Fe are found to induce superconductivity.^{6,21,22,27,28} However, no superconductivity is induced by Mn or Cr substitutions having a lower number of $3d$ electrons.^{23–26} On the other hand, isoelectronic substitution of Fe by the $4d$ transition metal Ru is also found to induce

the superconductivity.^{29,30} The common feature in the SC materials is that the long-range SDW order in the parent compounds must be largely suppressed before SC occurs as noted above, where, in addition, the AF spin fluctuations are still strong. The latter fact suggests an unconventional magnetic mechanism for the SC in the $FeAs$ -based materials. The extent and effects of electron and hole doping by such substitutions are still being debated.^{12,31,37,39–41}

While the effect of partial substitutions of Fe by transition metals has been investigated extensively, the physical properties of the end-point compounds AM_2As_2 of the $A(Fe_{1-x}M_x)_2As_2$ series are often not known in detail. Recently we reported crystallography and physical property studies of the end-point compounds $SrCu_2As_2$ and $CaCu_{1.7}As_2$ for $M = Cu$ which are sp -band metals.^{40,41} These compounds form in a collapsed tetragonal (cT) structure in which the formal oxidation state of As is $As^{-2} \equiv [As-As]^{-4/2}$ due to the interlayer $As-As$ bonding in the cT phase. Thus with the formal oxidation states of Sr and Ca taken to be $+2$, the Cu atoms in these cT compounds are then Cu^{+1} with a nonmagnetic $3d^{10}$ configuration as observed^{40,41} and also as previously predicted from electronic structure calculations for $SrCu_2As_2$ by Singh.⁴² Thus, extrapolating from high to low Cu concentrations, the electron or hole doping effect resulting from substitution of $M = Cu$ for Fe in $A(Fe_{1-x}M_x)_2As_2$ compounds is ambiguous and interesting.^{12,39,40}

To provide insight into the T - x phase diagrams of $A(Fe_{1-x}M_x)_2As_2$ systems with $M = Pd$, we report here our investigations of the crystallography and physical properties of single crystals of the three $(Ca,Sr,Ba)Pd_2As_2$ end-point compounds. $CaPd_2As_2$ and $SrPd_2As_2$ are reported to form in the body-centered tetragonal $ThCr_2Si_2$ -type structure (space group $I4/mmm$) and $BaPd_2As_2$ in the primitive tetragonal $CeMg_2Si_2$ -type structure (space group $P4/mmm$),^{43,44} as shown in Fig. 1 for $CaPd_2As_2$ and $BaPd_2As_2$. Both structures contain similar Pd square lattices. However, while the Ca

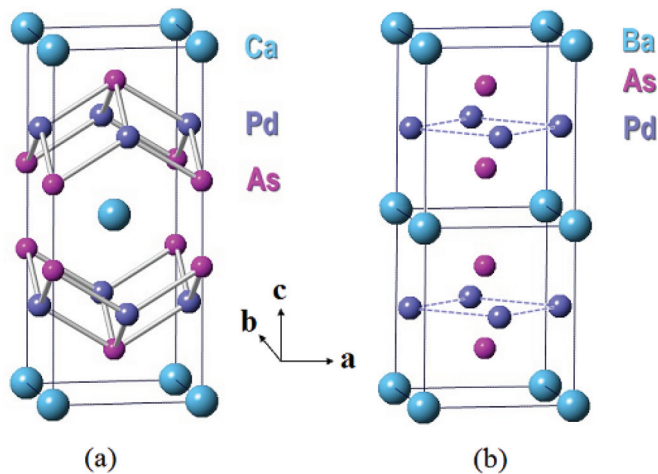


FIG. 1. (Color online) (a) A unit cell of ThCr_2Si_2 -type body-centered tetragonal crystal structure ($I4/mmm$) of CaPd_2As_2 and SrPd_2As_2 . (b) Two unit cells, stacked along the c axis, of the CeMg_2Si_2 -type primitive tetragonal crystal structure ($P4/mmm$) of BaPd_2As_2 .

atoms in CaPd_2As_2 form a body-centered tetragonal sublattice, in the BaPd_2As_2 structure the Ba atoms form a primitive tetragonal sublattice. Furthermore, the fourfold coordination of Pd by As is tetrahedral in CaPd_2As_2 but is planar rectangular in BaPd_2As_2 . The BaPd_2As_2 structure can be derived from that of CaPd_2As_2 by a $[\frac{1}{2}, \frac{1}{2}, 0]$ translation of the central As-Ca-As layer. Superconductivity was recently reported below $T_c = 3.0$ K in the similar compound SrPd_2Ge_2 with the ThCr_2Si_2 -type structure.⁴⁵

In this paper we report crystallographic investigations of crushed single crystal powders and physical property measurements of single crystals of the three (Ca,Sr,Ba) Pd_2As_2 compounds using magnetic susceptibility χ , isothermal magnetization M , specific heat C_p , ab -plane electrical resistivity ρ and magnetic penetration depth λ_{eff} measurements as a function of temperature T and applied magnetic field H . The published structures of these compounds are confirmed. The $\rho(T)$, $\chi(T)$, and $C_p(T)$ data demonstrate that all three compounds are sp -band-like metals. The $\chi(T)$ data indicate anisotropic diamagnetic behavior in all three compounds with $\chi_c > \chi_{ab}$ for CaPd_2As_2 and BaPd_2As_2 and $\chi_c < \chi_{ab}$ for SrPd_2As_2 . Bulk superconducting transitions at $T_c = 1.27(3)$ K for CaPd_2As_2 and $T_c = 0.92(5)$ K for SrPd_2As_2 are also reported together with other superconducting state properties derived from the above measurements. We analyzed the superconducting state electronic entropy and heat capacity data using our recent elaboration of the α -model of the BCS theory of superconductivity.⁴⁶ The data indicate that CaPd_2As_2 and SrPd_2As_2 are both conventional nodeless type-II electron-phonon superconductors, but with anisotropic s -wave gaps. Filamentary superconductivity was also detected below 2.0 K in BaPd_2As_2 .

The experimental details are described in Sec. II. The crystallographic studies of CaPd_2As_2 , SrPd_2As_2 , and BaPd_2As_2 are presented in Sec. III. The superconducting and normal-state properties of CaPd_2As_2 and SrPd_2As_2 are given in Secs. IV and V, respectively, and the measurements of their superconducting magnetic penetration depths versus temperature are presented in Sec. VI. The normal-state properties of BaPd_2As_2

are presented in Sec. VII. A summary of the experimental results and analyses and the conclusions is given in Sec. VIII.

II. EXPERIMENTAL DETAILS

Single crystals of APd_2As_2 ($A = \text{Ba}, \text{Ca}, \text{Sr}$) were grown using PdAs flux. The starting materials were high-purity elemental Ca (99.98%), Pd (99.998%), and As (99.99999%) from Alfa Aesar and Sr (99.95%) and Ba (99.99%) from Sigma Aldrich. The Ca, Sr, or Ba and prereacted PdAs flux taken in a 1:4 molar ratio were placed in alumina crucibles and sealed inside evacuated fused silica tubes. The sealed samples were heated to 1100 °C at a rate of 60–80 °C/h and held there for 12 h. After cooling at a rate of 2.5 °C/h to 800 °C, shiny platelike crystals of typical size $2 \times 1.5 \times 0.4$ mm³ were separated by decanting the flux with a centrifuge at that temperature.

The phase purity and the chemical composition of the CaPd_2As_2 , SrPd_2As_2 , and BaPd_2As_2 crystals were measured using a JEOL scanning electron microscope (SEM) equipped with an energy-dispersive x-ray analyzer (EDX). High-resolution SEM images demonstrated that the crystals were single phase. The EDX analyses of two or three single crystals of each compound were consistent with the ideal 1 : 2 : 2 stoichiometry. The crystal structures of the samples were determined by Rietveld refinements of powder x-ray diffraction (XRD) data for crushed single crystals collected on a Rigaku Geigerflex x-ray diffractometer using $\text{Cu } K_\alpha$ radiation. The Rietveld refinements were carried out using the FULLPROF software⁴⁷ which also confirmed the single-phase nature of the crystals.

The magnetization measurements were performed using a Quantum Design, Inc., superconducting quantum interference device magnetic properties measurement system (MPMS). We use Gaussian cgs units for the magnetic results and discussion, where the unit of magnetic field H is the Oe = G, but we also use the Tesla, with $1 \text{ T} \equiv 10^4 \text{ Oe}$, as a unit of convenience (the magnetic moment output by the MPMS software is in Gaussian cgs units where $1 \text{ emu} = 1 \text{ G cm}^3$).¹¹ In order to obtain the magnetic moment of the crystals in a particular field H we subtracted the precalibrated magnetic moment of the sample holder (quartz rod/plastic piece and GE varnish that were used to mount the sample for MPMS measurements) in the same H . Due to the small magnitudes of the magnetic moments of the small crystals and the uncertainty in the magnetic moment of the sample holder, the accuracy of the $M(H, T)$ and $\chi(T)$ data of the samples reported here is of order 10%.

The heat capacity measurements were carried out using the relaxation method in a Quantum Design, Inc., physical properties measurement system (PPMS). Temperatures down to 0.45 K were obtained using a ³He attachment to the PPMS. The ab -plane $\rho(T)$ measurements were performed by the standard four-probe ac technique using the ac transport option of the PPMS. The electrical leads were 25 μm diameter platinum wires attached to the crystals with EPO-TEK P1011 silver epoxy cured at 110 °C for 1 h. The accuracy of ρ is of order 10% due to uncertainties in the geometric factor.

The temperature variation of the magnetic penetration depth λ_{eff} was measured using a tunnel diode resonator (TDR) technique operating at about 15 MHz. The resonator consists

of an LC tank circuit with a single-layer coil of inductance $L \sim 1 \mu\text{H}$, a capacitor with capacitance $C \sim 100 \text{ pF}$, and a tunnel diode that is biased to the region of negative differential resistance, thus compensating the losses in the circuit. The circuit, therefore, self-oscillates at a frequency $f = (2\pi\sqrt{LC})^{-1}$. When a sample with magnetic susceptibility χ is inserted into the coil, the total inductance changes and the resonant frequency shifts accordingly by an amount which is proportional to χ . The temperature dependence of the resonance frequency shift $\Delta f(T)$ induced by changes in the sample's magnetic response is related to the magnetic susceptibility χ and hence $\lambda_{\text{eff}}(T)$ by^{48–50}

$$\Delta f(T) = -4\pi\chi(T)G$$

$$\approx -G \left\{ 1 - \frac{\lambda_{\text{eff}}(T)}{L_{\text{eff}}} \tanh \left[\frac{L_{\text{eff}}}{\lambda_{\text{eff}}(T)} \right] \right\}, \quad (1)$$

where G is a sample- and coil-dependent calibration constant and L_{eff} is the effective sample dimension.⁴⁸ The value of G is determined experimentally by pulling the sample out of the coil *in situ* and measuring the total associated frequency shift Δf_0 so that $\Delta\lambda_{\text{eff}}(T) = L_{\text{eff}} \delta f(T)/\Delta f_0$ where $\Delta\lambda_{\text{eff}}(T) = \lambda_{\text{eff}}(T) - \lambda_{\text{eff}}(T_{\text{min}})$, $\delta f(T) = f(T) - f(T_{\text{min}})$, and T_{min} is the minimum temperature of the measurement.⁴⁸ Another way to determine G is by matching the temperature dependence of the skin depth $d(T)$ obtained from the resonator response in the normal state to the measured resistivity $\rho(T)$ by using the relation $\delta(T) = (c/2\pi)\sqrt{\rho(T)/f}$.⁵¹ The ac magnetic field was applied along the c axis of single crystals of CaPd_2As_2 and SrPd_2As_2 , so the reported penetration depths are the respective values in the ab plane.

III. CRYSTALLOGRAPHY

The room temperature powder XRD patterns for crushed single crystals of CaPd_2As_2 , SrPd_2As_2 , and BaPd_2As_2 are shown in Figs. 2(a), 2(b), and 2(c), respectively. The weak unindexed peaks marked with stars for BaPd_2As_2 arise from the small amount of flux attached to the surface of the crystals prior to crushing them for the measurements. The Rietveld refinements confirmed the reported ThCr_2Si_2 -type body-centered tetragonal structure (space group $I4/mmm$) of CaPd_2As_2 and SrPd_2As_2 and the CeMg_2Si_2 -type primitive tetragonal structure (space group $P4/mmm$) of BaPd_2As_2 .^{43,44}

The refinement profiles for these structural models are shown in Fig. 2. During the final refinements, the thermal parameters B were set to $B = 0$ and the occupancies of the respective atomic sites were fixed to unity since there were no improvements in the quality of fits or significant changes in the lattice parameters or in the As c -axis position parameter z_{As} upon making small changes in B and in the occupancies. The crystallographic and refinement parameters are listed in Tables I and II. For comparison the lattice parameters and z_{As} values from the literature are also listed in Table I, where good agreement is found.

The c/a ratio and the interlayer As–As distance $d_{\text{As–As}} = (1 - 2z_{\text{As}})c$ for $(\text{Ca},\text{Sr})\text{Pd}_2\text{As}_2$ and $d_{\text{As–As}} = 2z_{\text{As}}c$ for BaPd_2As_2 are listed in Table I, where a “layer” is defined as an As–Pd–As slab in Fig. 1. The values of $d_{\text{As–As}}$ for CaPd_2As_2 and SrPd_2As_2 are close to the covalent single-bond distance of 2.38 \AA for As,⁵² indicating that these two compounds have

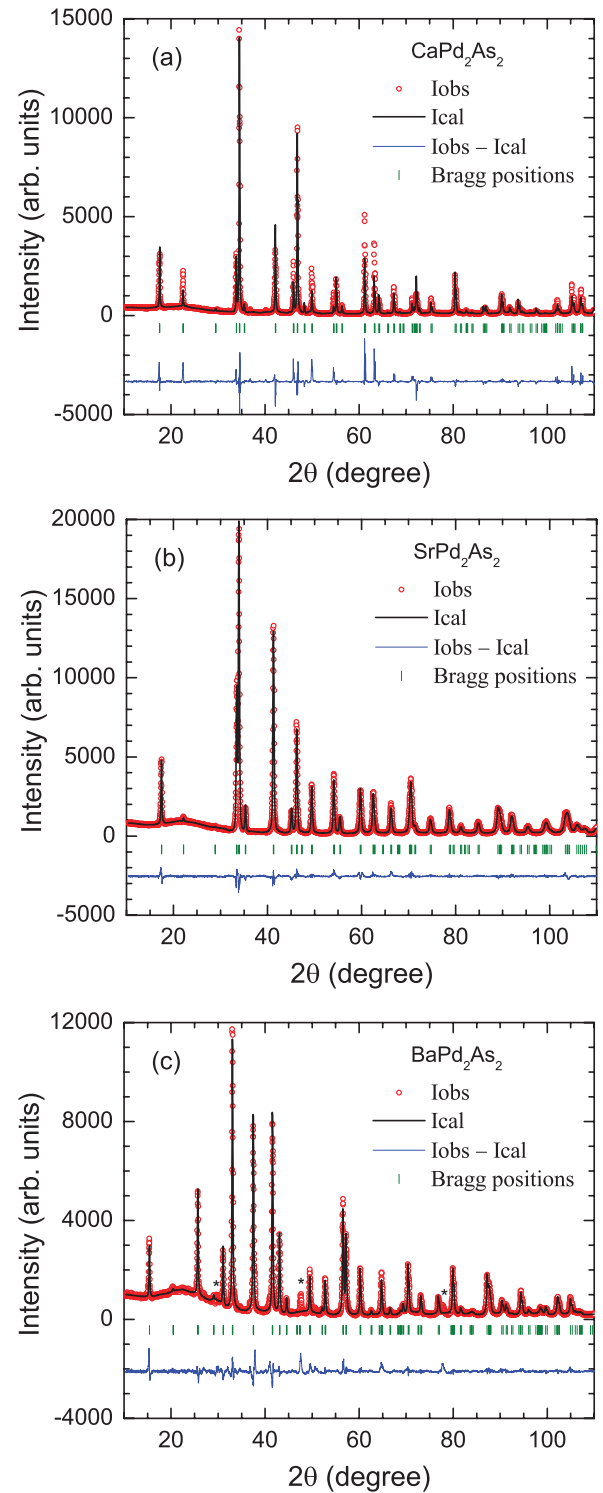


FIG. 2. (Color online) Powder x-ray diffraction patterns of (a) CaPd_2As_2 , (b) SrPd_2As_2 , and (c) BaPd_2As_2 recorded at room temperature. The solid lines through the experimental points are the Rietveld refinement profiles calculated [(a) and (b)] for the ThCr_2Si_2 -type body-centered tetragonal structure (space group $I4/mmm$), and (c) for the CeMg_2Si_2 -type primitive tetragonal structure (space group $P4/mmm$). In (a), (b), and (c), the short vertical bars mark the fitted Bragg peak positions. The lowermost curves represent the differences between the experimental and calculated intensities. The unindexed peaks marked with stars in (c) are peaks from residual PdAs flux on the surface of the samples.

TABLE I. Crystallographic and Rietveld refinement parameters obtained from powder XRD data for crushed APd₂As₂ (*A* = Ba, Ca, Sr) crystals. Error bars for the last digit of a quantity are given in parentheses and literature references are given in square brackets.

	CaPd ₂ As ₂	SrPd ₂ As ₂	BaPd ₂ As ₂
Structure	ThCr ₂ Si ₂ -type body-centered tetragonal	ThCr ₂ Si ₂ -type body-centered tetragonal	CeMg ₂ Si ₂ -type primitive tetragonal
Space group	<i>I4/mmm</i>	<i>I4/mmm</i>	<i>P4/mmm</i>
Formula units/unit cell (<i>Z</i>)	2	2	1
Lattice parameters			
<i>a</i> (Å)	4.2824(2) 4.299(1) [Ref. 43] 4.283(1) [Ref. 44]	4.3759(1) 4.383(1) [Ref. 43] 4.380(2) [Ref. 44]	4.3438(2) 4.346(1) [Ref. 43]
<i>c</i> (Å)	10.0880(4) 10.102(2) [Ref. 43] 10.093(1) [Ref. 44]	10.1671(3) 10.179(2) [Ref. 43] 10.169(1) [Ref. 44]	5.7536(2) 5.758(1) [Ref. 43]
<i>c/a</i>	2.3557(6)	2.3234(4)	1.3246(4)
<i>V</i> _{cell} (Å ³)	185.01(1)	194.69(1)	108.56(1)
As <i>c</i> -axis coordinate <i>z</i> _{As}	0.3763(3) 0.3796(2) [Ref. 43]	0.3768(1) 0.3766(2) [Ref. 43] 0.3768(1) [Ref. 44]	0.2705(4) 0.2700(8) [Ref. 43]
As–As interlayer distance <i>d</i> _{As–As} (Å)	2.496(7)	2.505(2)	3.113(4)
Theoretical density (g/cm ³)	7.230	7.682	7.648
Molar volume <i>V</i> _M (cm ³ /mol)	55.71	58.62	65.38
Refinement quality			
χ^2 (%)	11.8	3.68	8.09
<i>R</i> _p (%)	12.7	5.41	7.39
<i>R</i> _{wp} (%)	18.6	7.23	11.2

cT structures.⁴⁰ Therefore, as discussed in Sec. I, the formal oxidation state of Pd in these (Ca,Sr)Pd₂As₂ compounds is Pd⁺¹, which is the same formal oxidation state as for Cu in ThCr₂Si₂-type SrCu₂As₂.⁴⁰

IV. PHYSICAL PROPERTIES OF CaPd₂As₂ CRYSTALS

A. Electrical resistivity

The in-plane ρ of CaPd₂As₂ versus *T* is shown for crystal #1 at *H* = 0 in Fig. 3(a) and for crystal #2 under

TABLE II. Atomic coordinates obtained from the Rietveld refinements of powder XRD data for crushed APd₂As₂ (*A* = Ca, Sr, Ba) crystals.

Atom	Wyckoff symbol	<i>x</i>	<i>y</i>	<i>z</i>
CaPd ₂ As ₂ (<i>I4/mmm</i>)				
Ca	2a	0	0	0
Pd	4d	0	1/2	1/4
As	4e	0	0	0.3763(3)
SrPd ₂ As ₂ (<i>I4/mmm</i>)				
Sr	2a	0	0	0
Pd	4d	0	1/2	1/4
As	4e	0	0	0.3768(1)
BaPd ₂ As ₂ (<i>P4/mmm</i>)				
Ba	1a	0	0	0
Pd	2e	0	1/2	1/2
As	2h	1/2	1/2	0.2705(4)

various *H* in Fig. 3(b). A sharp zero-field superconducting transition is observed in Fig. 3(b) at *T*_c = 1.28(3) K that is suppressed by *H* = 0.14 T to below 0.45 K. For crystal #1, the superconducting onset is also at 1.8 K as shown in the inset of Fig. 3(a). A broad superconducting transition was seen in another crystal (#3) with an onset at 1.8 K and zero resistance at 1.3 K (not shown). Interestingly, the $\rho(T)$ of crystal #2 in Fig. 3(b) exhibits an upturn and peak before the resistivity drops due to superconductivity which is suppressed by a field *H* ≥ 0.08 T. The origin of this $\rho(T)$ peak is not clear. For crystal #1 the residual resistivity at 2 K before entering the superconducting state is $\rho_0 = 43 \mu\Omega \text{ cm}$ and the residual resistivity ratio is $\text{RRR} \equiv \rho(300 \text{ K})/\rho(2 \text{ K}) \approx 3$.

In the following we fit the normal-state $\rho(T)$ data by the Bloch-Grüneisen (BG) model which describes the electrical resistivity $\rho_{\text{BG}}(T)$ due to scattering of the charge carriers by longitudinal acoustic lattice vibrations in the absence of Umklapp scattering, given by^{53,54}

$$\rho_{\text{BG}}(T/\Theta_{\text{R}}) = 4\mathcal{R} \left(\frac{T}{\Theta_{\text{R}}} \right)^5 \int_0^{\Theta_{\text{R}}/T} \frac{x^5}{(e^x - 1)(1 - e^{-x})} dx, \quad (2a)$$

where Θ_{R} is the Debye temperature obtained from fitting resistivity measurements, \mathcal{R} is a material-dependent prefactor that is independent of *T*, and

$$\rho_{\text{BG}}(T/\Theta_{\text{R}} = 1) = 0.9464635 \mathcal{R}. \quad (2b)$$

The experimental $\rho(T)$ data are fitted by

$$\rho(T) = \rho_0 + \rho(\Theta_{\text{R}})\rho_{\text{n}}(T/\Theta_{\text{R}}), \quad (2c)$$

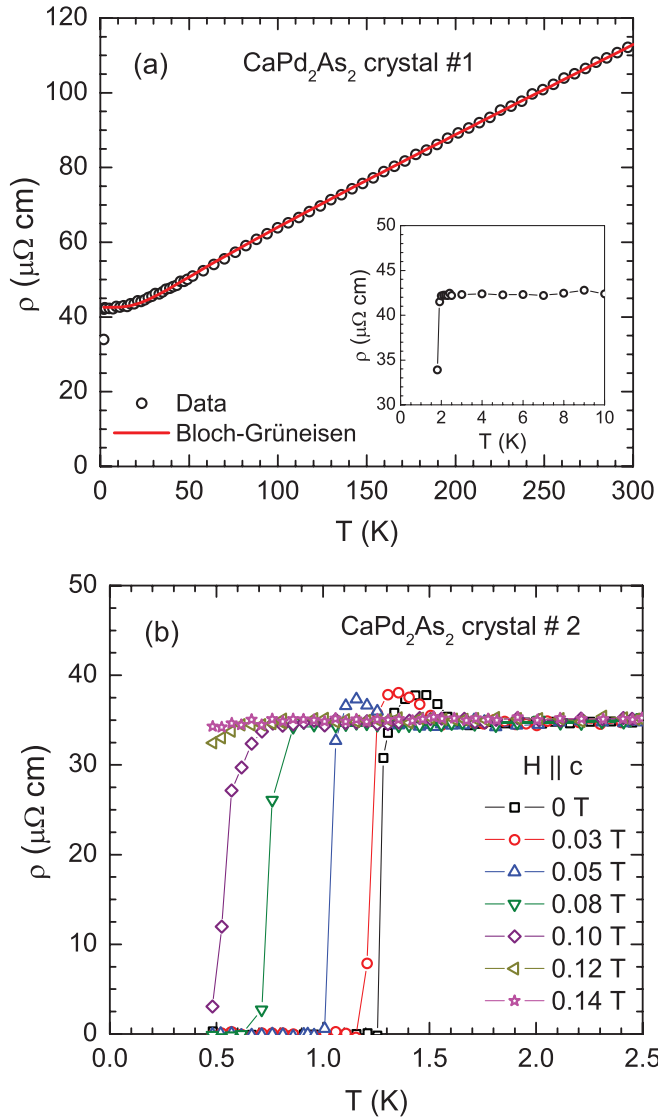


FIG. 3. (Color online) (a) In-plane electrical resistivity ρ of a CaPd_2As_2 crystal #1 versus temperature T measured in applied magnetic field $H = 0$. The red curve is a fit by the Bloch-Grüneisen model in the T range 2–300 K. Inset: Expanded plot of $\rho(T)$ below 10 K to show the onset of superconductivity at 2.0 K. (b) Expanded plot of $\rho(T)$ of CaPd_2As_2 crystal #2 for $0.45 \text{ K} \leq T \leq 2.5 \text{ K}$ showing the superconducting transition for different values of H , as listed, applied along the c axis.

where Eq. (2a) yields the normalized dimensionless BG resistivity

$$\rho_n(T/\Theta_R) = 4.226259 \left(\frac{T}{\Theta_R} \right)^5 \times \int_0^{\Theta_R/T} \frac{x^5}{(e^x - 1)(1 - e^{-x})} dx. \quad (2d)$$

An excellent fit of the $\rho(T)$ data by Eqs. (2) was obtained using the three independent fitting parameters ρ_0 , $\rho(\Theta_R)$, and Θ_R for $2 \text{ K} \leq T \leq 300 \text{ K}$, as shown by the red curve in Fig. 3(a). The single parameter Θ_R determines the T dependence of the fit. While fitting the $\rho(T)$ data we used the analytic Padé approximant function $\rho_n(T/\Theta_R)$ in

TABLE III. Parameters derived from Bloch-Grüneisen fits to the resistivities ρ within the ab plane of the listed single crystals obtained using Eqs. (2). Here ρ_0 is the residual resistivity extrapolated to $T = 0$, Θ_R is the Debye temperature determined from resistivity measurements, $\rho(\Theta_R)$ is the fitted value of ρ at $T = \Theta_R$, and \mathcal{R} is obtained from the fitted value of $\rho(\Theta_R)$ using Eq. (2b). The ρ and \mathcal{R} values do not take into account the systematic error of order 10% arising from uncertainties in the geometric factor required to calculate ρ of a crystal from its measured resistance. The accuracy of Θ_R is not affected by this systematic error since this parameter is determined solely from the T dependence of ρ .

Compound	ρ_0 ($\mu\Omega \text{ cm}$)	Θ_R (K)	$\rho(\Theta_R)$ ($\mu\Omega \text{ cm}$)	\mathcal{R} ($\mu\Omega \text{ cm}$)
CaPd_2As_2	42.60(7)	135(3)	30.3(5)	32.0
SrPd_2As_2	7.57(6)	170(3)	27.6(5)	29.2
BaPd_2As_2	1.02(1)	114(1)	8.84(1)	9.34

place of Eq. (2d) developed in Ref. 54 which accurately describes $\rho_n(T/\Theta_R)$ and greatly simplifies least-squares fitting of experimental $\rho(T)$ data by the BG theory. The fitting parameters are summarized in Table III along with those of the other two compounds discussed below. The \mathcal{R} value is obtained from the fitted value of $\rho(\Theta_R)$ using Eq. (2b).

B. Heat capacity

1. Overview of the superconducting and normal-state heat capacity

The $C_p(T)$ of a CaPd_2As_2 crystal is shown in Fig. 4 for $0.45 \text{ K} \leq T \leq 300 \text{ K}$. As shown in the expanded plot of the low- T data in the inset of Fig. 4, a sharp jump is observed in $C_p(T)$ due to the occurrence of superconductivity at

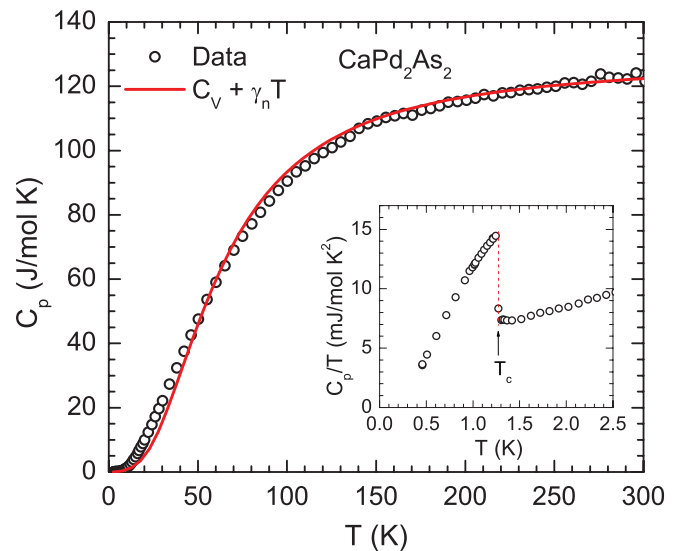


FIG. 4. (Color online) The heat capacity C_p of a CaPd_2As_2 single crystal [crystal #2 of Fig. 3(b)] versus temperature T for $2.5 \text{ K} \leq T \leq 300 \text{ K}$ measured in zero magnetic field. The red solid curve is the fitted sum of the contributions from the Debye lattice heat capacity $C_V^{\text{Debye}}(T)$ and predetermined electronic heat capacity $\gamma_n T$ according to Eq. (5a). Inset: C_p/T vs T for $0.45 \text{ K} \leq T \leq 2.5 \text{ K}$. The dotted red vertical line indicates the T_c .

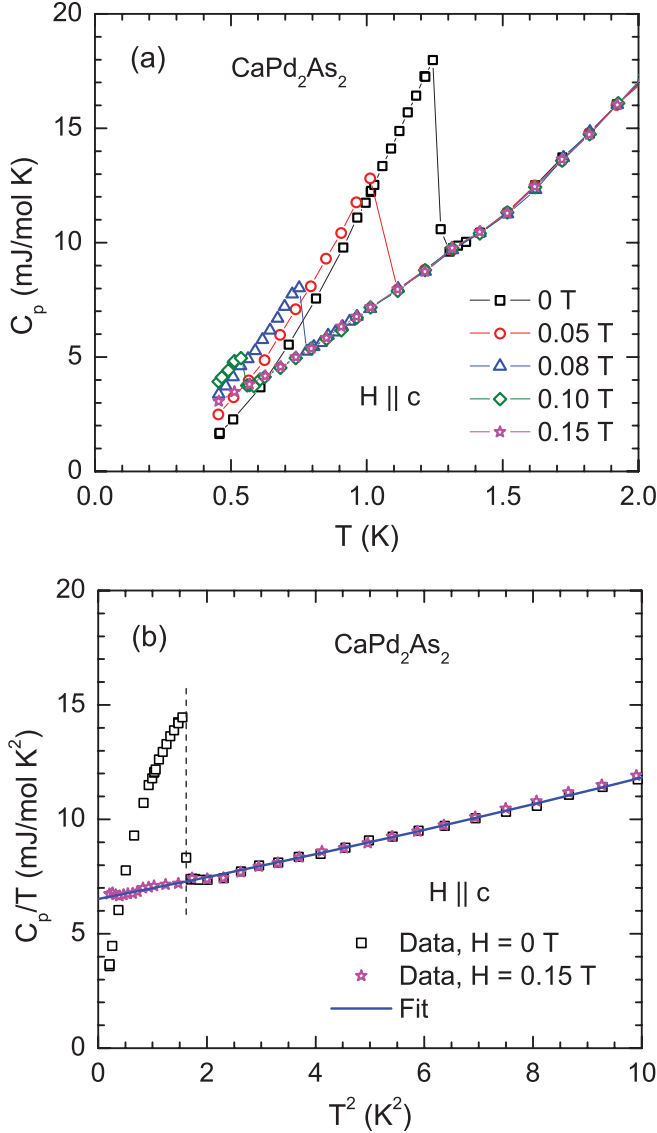


FIG. 5. (Color online) (a) Heat capacity C_p versus temperature T of a CaPd_2As_2 single crystal [crystal #2 of Fig. 3(b)] for $0.45 \text{ K} \leq T \leq 2.0 \text{ K}$ measured in different magnetic fields H applied along the c axis. (b) C_p/T versus T^2 for $0.45 \text{ K} \leq T \leq 3.2 \text{ K}$ with $H = 0$ and 0.15 T . The blue curve is a fit of the $H = 0.15 \text{ T}$ data for $0.45 \text{ K} \leq T \leq 4.5 \text{ K}$ together with the $H = 0$ data for $1.5 \text{ K} \leq T \leq 4.5 \text{ K}$ by Eq. (3).

$T_c = 1.27(3) \text{ K}$. The $C_p(T)$ data measured under various H are shown in Fig. 5(a). These data show that the T_c decreases with increasing H and is suppressed to below 0.45 K by $H = 0.15 \text{ T}$.

Plots of C_p/T versus T^2 for $H = 0$ and 0.15 T are shown in Fig. 5(b). We analyzed the normal-state $C_p(T)$ data at $0.45 \text{ K} \leq T \leq 4.5 \text{ K}$ for $H = 0.15 \text{ T}$ and the data at $1.5 \text{ K} \leq T \leq 4.5 \text{ K}$ for $H = 0$ together according to

$$\frac{C_p(T)}{T} = \gamma_n + \beta T^2 + \delta T^4, \quad (3)$$

where γ_n is the normal-state Sommerfeld electronic heat capacity coefficient, β is the Debye T^3 -law lattice heat capacity coefficient, and δT^4 is a higher-order lattice contribution. A fit of the normal-state data by Eq. (3), shown as the blue curve

in Fig. 5(b), gives $\gamma_n = 6.52(2) \text{ mJ/mol K}^2$, $\beta = 0.463(6) \text{ mJ/mol K}^4$, and $\delta = 6.8(4) \mu\text{J/mol K}^6$. We estimate the Debye temperature Θ_D from β using the relation⁵⁵

$$\Theta_D = \left(\frac{12\pi^4 R n}{5\beta} \right)^{1/3}, \quad (4)$$

where R is the molar gas constant and $n = 5$ is the number of atoms per formula unit (f.u.), yielding $\Theta_D = 276(1) \text{ K}$.

The measured normal-state $C_p(T = 300 \text{ K}) = 123 \text{ J/mol K}$ in Fig. 4 is close to the expected classical Dulong-Petit high- T limiting value $C_V = 3nR = 15R = 124.7 \text{ J/mol K}$ at constant volume due to acoustic lattice vibrations.^{55,56} Our normal-state $C_p(T)$ data for the T range $2.5 \text{ K} \leq T \leq 300 \text{ K}$ were fitted by the sum of the above electronic term $\gamma_n T$ and the Debye model lattice heat capacity $C_{V \text{ Debye}}(T)$ per mole of atoms due to acoustic lattice vibrations according to

$$C_p(T) = \gamma_n T + n C_{V \text{ Debye}}(T/\Theta_D), \quad (5a)$$

where⁵⁶

$$C_{V \text{ Debye}}(T/\Theta_D) = 9R \left(\frac{T}{\Theta_D} \right)^3 \int_0^{\Theta_D/T} \frac{x^4 e^x}{(e^x - 1)^2} dx \quad (5b)$$

and

$$C_{V \text{ Debye}}(T/\Theta_D = 1) = 9R \int_0^1 \frac{x^4 e^x}{(e^x - 1)^2} dx \quad (5c) \\ \approx 2.8552 R.$$

The integral in Eq. (5c) can be obtained in closed form but the expression is cumbersome. When carrying out the least-squares fit of the experimental $C_p(T)$ data by Eqs. (5) we used the high-accuracy analytic Padé approximant for $C_{V \text{ Debye}}(T/\Theta_D)$ in Eq. (5b) which we formulated in Ref. 54 that greatly simplifies the fit. The fit was carried out using the fixed value $\gamma_n = 6.52 \text{ mJ/mol K}^2$ obtained above. Thus, Θ_D is the only adjustable parameter. The fit yielded $\Theta_D = 252(2) \text{ K}$ and is shown by the red curve in Fig. 4. This value of Θ_D is close to but slightly smaller than the value $\Theta_D = 276(1) \text{ K}$ obtained above from analysis of the low- T C_p data. Such differences are expected due to the T dependence of Θ_D .^{54,56}

We estimate the density of states at the Fermi energy for both spin directions obtained from heat capacity measurements $\mathcal{D}_C(E_F)$ using the relation⁵⁵

$$\gamma_n = \frac{\pi^2 k_B^2}{3} \mathcal{D}_C(E_F). \quad (6)$$

This $\mathcal{D}_C(E_F)$ contains the enhancement from the many-body electron-phonon interaction $\lambda_{\text{el-ph}}$. This is also the density of states that enters the BCS equations for T_c and for the BCS gap and thermodynamic properties versus T . Using the above γ_n value gives

$$\mathcal{D}_C(E_F) = 2.76 \text{ states/eV f.u.} \quad (7)$$

The enhancements of the bare (band structure) density of states $\mathcal{D}_{\text{band}}(E_F)$ and the bare effective mass m_{band}^* due to the electron-phonon interaction are⁵⁷

$$\mathcal{D}_C(E_F) = \mathcal{D}_{\text{band}}(E_F)(1 + \lambda_{\text{el-ph}}), \quad (8a)$$

$$m^* = m_{\text{band}}^*(1 + \lambda_{\text{el-ph}}), \quad (8b)$$

where $\lambda_{\text{el-ph}}$ is the electron-phonon coupling constant.

TABLE IV. The linear specific heat coefficients γ_n and the coefficients β and δ of the T^3 and T^5 terms in the low- T heat capacity, respectively, and the density of states at the Fermi energy $\mathcal{D}_C(E_F)$ and $\mathcal{D}_{\text{band}}(E_F)$ for both spin directions for CaPd_2As_2 , SrPd_2As_2 , and BaPd_2As_2 single crystals. The Debye temperatures Θ_D obtained at low T and for all T from heat capacity measurements and the Debye temperature Θ_R obtained from fitting electrical resistivity data, respectively, are also listed.

Compound	γ_n (mJ/mol K ²)	β (mJ/mol K ⁴)	δ ($\mu\text{J}/\text{mol K}^6$)	$\mathcal{D}_C(E_F)$ (states/eV f.u.)	$\mathcal{D}_{\text{band}}(E_F)$ (states/eV f.u.)	Θ_D (K) from low T	Θ_D (K) from all T	Θ_R (K) from $\rho(T)$
CaPd_2As_2	6.52(2)	0.463(6)	6.8(4)	2.76(1)	1.87(1)	276(1)	252(2)	135(3)
SrPd_2As_2	6.43(3)	0.369(8)	3.7(5)	2.73(2)	1.89(1)	298(3)	245(3)	170(3)
BaPd_2As_2	4.79(2)	0.638(5)	4.0(3)	2.03(1)		248(1)	227(2)	114(1)

The $\lambda_{\text{el-ph}}$ value can be estimated from McMillan's theory⁵⁸ for the electron-phonon mechanism of superconductivity and is related to Θ_D and T_c by

$$\lambda_{\text{el-ph}} = \frac{1.04 + \mu^* \ln(\Theta_D/1.45 T_c)}{(1 - 0.62\mu^*) \ln(\Theta_D/1.45 T_c) - 1.04}. \quad (9)$$

Here μ^* is the repulsive screened Coulomb parameter having a value often between 0.1 and 0.15 and is usually taken as $\mu^* = 0.13$. With this value of μ^* together with $T_c = 1.27$ K and $\Theta_D = 276$ K as determined above (Table IV), Eqs. (8a) and (9) yield

$$\lambda_{\text{el-ph}} = 0.474, \quad \mathcal{D}_{\text{band}}(E_F) = 1.87(1) \text{ states/eV f.u.} \quad (10)$$

The relatively small value of $\lambda_{\text{el-ph}}$ implies weak-coupling superconductivity in CaPd_2As_2 .

A difference of μ^* from the assumed value of 0.13 would give a different value of the calculated $\lambda_{\text{el-ph}}$. For example, from Eq. (9) we obtain $\lambda_{\text{el-ph}} = 0.421$ if $\mu^* = 0.10$ and $\lambda_{\text{el-ph}} = 0.511$ if $\mu^* = 0.15$. Such differences would result in corresponding differences in the calculated $\mathcal{D}_{\text{band}}(E_F)$. However, our value of $\mathcal{D}_{\text{band}}(E_F)$ obtained below for the Sr compound using $\mu^* = 0.13$ (Table IV) precisely agrees with the value $\mathcal{D}_{\text{band}}(E_F) = 1.93$ states/eV f.u. for both spin directions obtained from band calculations for this compound in the reference cited in the *Note added* at the end of this paper. This agreement also indicates that electron correlation effects are not large, consistent with the sp -band-like nature of the APd_2As_2 compounds that we deduce from the normal-state data.

The values of $\mathcal{D}_C(E_F)$, m^* , and ρ_0 can be used to estimate the Fermi velocity (speed) v_F and the mean-free path ℓ for conduction carrier scattering at low T . In a single-band quasi-free-electron Fermi gas model, v_F is⁵⁵

$$v_F = \frac{\pi^2 \hbar^3}{m^* V_{\text{f.u.}}} \mathcal{D}_C(E_F) \quad (11a)$$

$$= \frac{\pi^2 \hbar^3}{m^* V_{\text{f.u.}}} \mathcal{D}_{\text{band}}(E_F) (1 + \lambda_{\text{el-ph}}), \quad (11b)$$

where $V_{\text{f.u.}} = V_{\text{cell}}/2$ from Table I is the volume per formula unit and \hbar is Planck's constant divided by 2π . Assuming $m_{\text{band}}^* = m_e$ where m_e is the free-electron mass,⁵⁹ Eqs. (8b) and (11a) yield

$$v_F = 1.20 \times 10^8 \text{ cm/s.} \quad (12)$$

The mean-free path $\ell = v_F \tau$, where τ is the mean-free scattering time, is obtained from v_F using⁵⁵

$$\ell = 3\pi^2 \left(\frac{\hbar}{e^2 \rho_0} \right) \left(\frac{\hbar}{m^* v_F} \right)^2, \quad (13)$$

where $\hbar/e^2 = 4108 \Omega$. From Eqs. (8), (11a), and (13), the value of $m^* v_F$ and hence of ℓ is independent of $\lambda_{\text{el-ph}}$. Using $\rho_0 = 34.6 \mu\Omega \text{ cm}$ (for crystal No. 2), $m_{\text{band}}^* = m_e$ and the value of v_F in Eq. (12), Eqs. (8b) and (13) give

$$\ell = 1.52 \text{ nm}, \quad (14)$$

which is only 3.6 in-plane lattice constants (Table I).

The plasma angular frequency ω_p of the conduction carriers can be estimated using the quasi-free-electron single-band relation

$$n = \frac{1}{3\pi^2} \left(\frac{m^* v_F}{\hbar} \right)^3, \quad (15)$$

yielding⁵⁵

$$\omega_p^2 = \frac{4\pi n e^2}{m^*} = \frac{4(m^* e)^2 (v_F/\hbar)^3}{3\pi}. \quad (16)$$

Using Eq. (8b), $m_{\text{band}}^* = m_e$ and v_F from Eq. (12) gives

$$\omega_p = 1.61 \times 10^{16} \text{ rad/s.} \quad (17)$$

The superconducting London penetration depth in the clean limit at $T = 0$, $\lambda_L(0)$, is a normal-state property given by^{46,60}

$$\lambda_L(0) = \frac{c}{\omega_p}, \quad (18)$$

where c is the speed of light in vacuum. The value of ω_p in Eq. (17) gives

$$\lambda_L(0) = 1.86 \times 10^{-6} \text{ cm} = 18.6 \text{ nm.} \quad (19)$$

However, we will see in the following section that CaPd_2As_2 is in the dirty limit and not in the clean limit that was treated by BCS, where the actual penetration depth $\lambda_{\text{eff}}(0)$ is much larger than $\lambda_L(0)$.

The normal-state parameters obtained from the above analyses of $C_p(T)$ for CaPd_2As_2 are summarized in Tables IV and V together with those obtained below for the other two compounds discussed in this paper.

The Debye temperatures Θ_R in Table III obtained for the three compounds from analyses of the respective $\rho(T)$ data are also listed in Table IV for comparison. The large discrepancies

between the values of Θ_D and Θ_R for each compound indicate that the assumptions⁵⁴ of the BG theory are violated in the APd_2As_2 compounds. The BG theory ignores Umklapp carrier scattering; if the Fermi wave vector k_F is significantly smaller than the Debye wave vector k_D , one might expect Θ_D and Θ_R to be significantly different; and a mechanism such as electron-electron scattering in addition to the electron-phonon scattering assumed in the BG theory could contribute to the T dependence of ρ .

2. Superconducting state properties

The electronic contribution $C_e(T)$ to $C_p(T)$ of CaPd_2As_2 obtained at low T by subtracting the low- T phonon contribution $\beta T^3 + \delta T^5$ from $C_p(T)$ is shown in Fig. 6(a). The large sharp jump ΔC_e in C_e at $T_c = 1.27(3)$ K indicates that the superconductivity in CaPd_2As_2 is a bulk effect, confirmed below. The vertical heat capacity jump indicated by the vertical dotted line in Fig. 6(b) yields $\Delta C_e/T_c = 7.4(2)$ mJ/mol K² and hence $\Delta C_e = 9.4(3)$ mJ/mol K. Using the normal-state $\gamma_n = 6.52(2)$ mJ/mol K² from Table IV, one obtains $\Delta C_e/\gamma_n T_c = 1.14(3)$ which is much smaller than the BCS value $\Delta C_e/\gamma_n T_c = 1.43$ in the weak-coupling limit.^{46,60} Because the bulk superconducting transition in $C_e(T)$ is very sharp, we infer that the reduction in $\Delta C_e/\gamma_n T_c$ from the BCS value is intrinsic. This reduction can happen if the superconducting gap (order parameter) is anisotropic in wave vector space, either from anisotropy in the gap on a single Fermi surface⁴⁶ or from multiple bands with distinct Fermi surfaces, each with a different isotropic or anisotropic gap,⁶¹ as discussed in the context of the α -model below.

3. Value of α within the α -model

For simplicity, we analyze the zero-field superconducting state thermodynamic data for CaPd_2As_2 within the framework of the so-called α -model of the BCS theory of superconductivity,^{46,62,63} where $\alpha \equiv \Delta(0)/k_B T_c$. In this model the normalized gap $\tilde{\Delta}(T) \equiv \Delta(T)/\Delta(0)$ is the same as in the BCS theory which is calculated from the BCS gap equation^{46,62} with $\alpha = \alpha_{\text{BCS}}$ where

$$\alpha_{\text{BCS}} = \pi e^{-\gamma_E} \approx 1.7639 \quad (20)$$

and $\gamma_E \approx 0.5772$ is Euler's constant. However, for calculating the thermodynamic properties, one uses a variable α parameter, which represents an inconsistency in the model, but which allows one to fit superconducting state thermodynamic data that deviate from the BCS predictions. The superconducting and normal state electronic entropies at T_c are the same, as in the BCS model, so the superconducting transition is still second order with no latent heat. One can interpret the quantitatively determined deviations from the BCS predictions in terms of other models and theories. For example, values $\alpha > \alpha_{\text{BCS}}$ can arise from the presence of strong electron-phonon coupling in contrast to the weak-coupling assumption in the BCS theory,⁶⁴ whereas $\alpha < \alpha_{\text{BCS}}$ can occur from gap anisotropy in momentum space⁴⁶ which we therefore assume is responsible for the reduced heat capacity jump in CaPd_2As_2 compared to the BCS theory prediction.

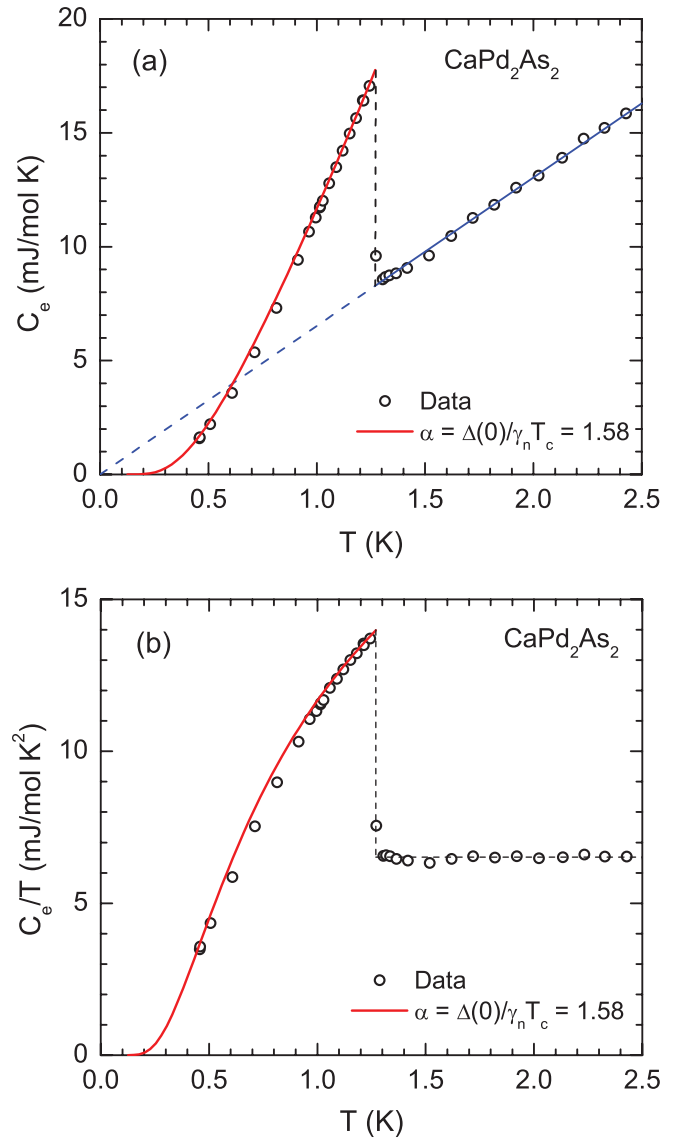


FIG. 6. (Color online) (a) Electronic contribution C_e to the heat capacity versus temperature T of CaPd_2As_2 . (b) C_e/T versus T . The solid red curve in each figure is the theoretical prediction of the α -model in Eq. (23a) for $\alpha = 1.58$. The BCS value is $\alpha_{\text{BCS}} \approx 1.764$. The normal-state heat capacity is $C_{\text{en}} = \gamma_n T$ with $\gamma_n = 6.52$ mJ/mol K². In (a), this normal-state contribution is the blue straight line and the extrapolation to low T is the dashed blue line. In (b), the normal-state behavior is $C_{\text{en}}/T = \gamma_n$.

The value of α is related to the heat capacity jump at T_c by⁴⁶

$$\begin{aligned} \frac{\Delta C_e(T_c)}{\gamma_n T_c} &= \frac{\Delta C_e(T_c)}{\gamma_n T_c} \Big|_{\text{BCS}} \left(\frac{\alpha}{\alpha_{\text{BCS}}} \right)^2 \\ &= \frac{12}{7\zeta(3)} \left(\frac{\alpha}{\alpha_{\text{BCS}}} \right)^2 \approx 1.426 \left(\frac{\alpha}{\alpha_{\text{BCS}}} \right)^2, \end{aligned} \quad (21)$$

where $\zeta(x)$ is the Riemann zeta function. Inserting our normalized experimental heat capacity jump value into Eq. (21) gives

$$\alpha = 1.58(2), \quad (22)$$

which is significantly smaller than the BCS value of 1.764.

The temperature dependence of the superconducting state electronic heat capacity is calculated within the α -model using⁴⁶

$$\frac{C_{es}(t)}{\gamma_n T_c} = \frac{6\alpha^3}{\pi^2 t} \int_0^\infty f(1-f) \left(\frac{\tilde{E}^2}{t} - \frac{1}{2} \frac{d\tilde{\Delta}^2}{dt} \right) d\tilde{\epsilon}, \quad (23a)$$

where $t = T/T_c$, the normalized normal-state electron energy is $\tilde{\epsilon} = \epsilon/\Delta(0)$, the normalized excited quasiparticle (electron and hole) energy is

$$\tilde{E} = \frac{E}{\Delta(0)} = \sqrt{\tilde{\epsilon}^2 + \tilde{\Delta}^2}, \quad (23b)$$

and the Fermi-Dirac distribution function in the dimensionless variables is (with $E_F \equiv 0$)

$$f \equiv f(\alpha, \tilde{E}, t) = \frac{1}{e^{\alpha \tilde{E}/t} + 1}$$

with

$$\frac{E}{k_B T} = \frac{\alpha \tilde{E}}{t}. \quad (23c)$$

The t -dependent $\tilde{\Delta}(t)$ and $d\tilde{\Delta}(t)/dt^2$ are calculated as described in Ref. 46.

The solid red curves in Figs. 6(a) and 6(b) are the theoretical predictions for $C_{es}(T)$ and $C_{es}(T)/T$, respectively, calculated from Eqs. (23) using $\alpha = 1.58$ and are seen to be in good agreement with the data. The agreement of the lowest- T data with the theory indicates that there is no residual electronic specific heat for $T \rightarrow 0$, which in turn indicates that the entire sample is superconducting with a single nodeless s -wave gap and with a single T_c . Because $\alpha < \alpha_{BCS} \approx 1.764$, we infer that the s -wave order parameter is anisotropic in momentum space as discussed above.⁴⁶

4. Thermodynamic critical field H_c

The experimental thermodynamic critical field H_c versus T of a superconductor can be estimated using the zero-field $C_e(T)$ data via the electronic entropy difference between the normal (S_{en}) and superconducting (S_{es}) states per unit volume at $H = 0$ according to the Clausius-Clapeyron-type relation^{60,65}

$$S_{en}(T) - S_{es}(T) = -\frac{1}{8\pi} \frac{dH_c^2(T)}{dT}, \quad (24a)$$

which, with $S_e(T') = \int_0^{T'} [C_e(T'')/T''] dT''$, yields

$$H_c^2(T) = 8\pi \int_T^{T_c} [S_{en}(T') - S_{es}(T')] dT'. \quad (24b)$$

In cgs units, H_c is expressed in units of Oe, where $1 \text{ Oe}^2 = 1 \text{ erg/cm}^3$, so $S_{en}(T') = \gamma_{nV} T'$ is in units of $\text{erg/cm}^3 \text{ K}$. The Sommerfeld coefficient γ_{nV} in units of $\text{erg/cm}^3 \text{ K}^2$ is calculated from the above Sommerfeld coefficient γ_n in units of $\text{mJ/mol K}^2 = 10^4 \text{ erg/mol K}^2$ according to

$$\gamma_{nV} = \frac{\gamma_n}{V_M}, \quad (25)$$

where V_M is the molar volume in units of cm^3/mol . For CaPd_2As_2 , our values $\gamma_n = 6.52 \text{ mJ/mol K}^2$ and $V_M = 55.7 \text{ cm}^3/\text{mol}$ from Table I give $\gamma_{nV} = 1170 \text{ erg/cm}^3 \text{ K}^2$. The

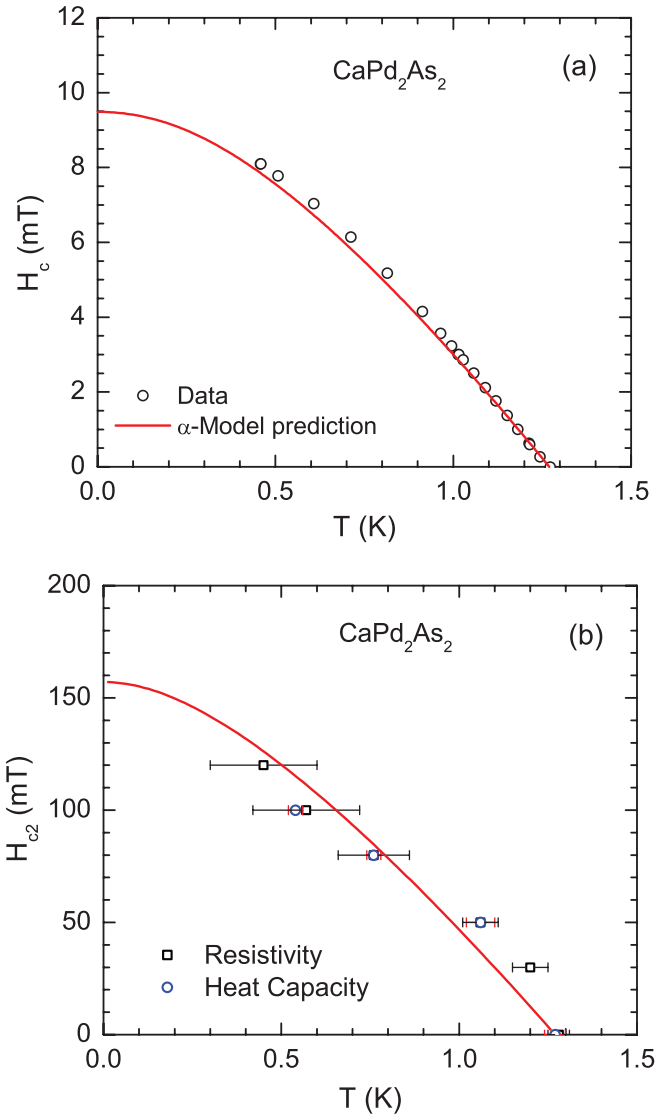


FIG. 7. (Color online) (a) Thermodynamic critical field H_c versus temperature T obtained for CaPd_2As_2 from the experimentally derived electronic heat capacity $C_e(T)$ data using Eqs. (24) (open circles) and the theoretical prediction of the α -model (Refs. 46 and 63) using $T_c = 1.27 \text{ K}$, $\alpha = 1.58$ and $\gamma_n = 6.52 \text{ mJ/mol K}^2$ in Eqs. (26) and (27) (red curve). (b) Upper critical magnetic field $H_{c2}(T)$ of CaPd_2As_2 determined from the electrical resistivity $\rho(T, H)$ (black open squares) and heat capacity $C_p(T, H)$ (blue open circles) data in Figs. 3(b) and 5(a), respectively. The red curve is the prediction for $H_{c2}(T)$ by the WHH theory (Ref. 67) in Eqs. (32) for $dH_{c2}(T)/dT|_{T=T_c} = -0.18 \text{ T/K}$, $\alpha_M = 0.13$ and $\lambda_{so} = 0$.

experimental $H_c(T)$ data obtained from Eqs. (24) are plotted as open circles in Fig. 7(a).

In the α -model, the thermodynamic critical field at $T = 0$ is given by⁴⁶

$$\frac{H_c(0)}{(\gamma_{nV} T_c^2)^{1/2}} = \sqrt{\frac{6}{\pi}} \alpha \approx 1.382 \alpha. \quad (26)$$

Using our values of γ_{nV} , $\alpha = 1.58$ and $T_c = 1.27 \text{ K}$ gives $H_c(0) = 9.5 \text{ mT}$. The T dependence of H_c is calculated

from⁴⁶

$$\begin{aligned}\frac{H_c^2(t)}{H_c^2(0)} &= \frac{4\pi^2}{3\alpha^2} \int_t^1 \left[\frac{S_{\text{en}}(t')}{\gamma_{\text{NV}} T_c} - \frac{S_{\text{es}}(t')}{\gamma_{\text{NV}} T_c} \right] dt' \\ &= \frac{4\pi^2}{3\alpha^2} \int_t^1 \left[t' - \frac{S_{\text{es}}(t')}{\gamma_{\text{NV}} T_c} \right] dt',\end{aligned}\quad (27a)$$

where the normal-state electronic entropy is $S_{\text{en}}(t')/\gamma_{\text{NV}} T_c = t'$, and the superconducting state entropy is calculated from⁴⁶

$$\frac{S_{\text{es}}(t)}{\gamma_{\text{NV}} T_c} = \frac{6\alpha^2}{\pi^2 t} \int_0^\infty f(\alpha, \tilde{E}, t) \left(\tilde{E} + \frac{\tilde{\epsilon}^2}{\tilde{E}} \right) d\tilde{\epsilon}. \quad (27b)$$

The resulting $H_c(T)$ calculated for the above values of $H_c(0)$, α , γ_{NV} , and T_c is shown by the red curve in Fig. 7(a). Good agreement is observed between the temperature dependence of the data and the theoretical prediction of the α -model, although the calculated zero-temperature value appears to be a bit low.

5. Upper critical field H_{c2}

The $\rho(T)$ data in Fig. 3(b) and the $C_p(T)$ data in Fig. 5(a) for CaPd_2As_2 in fields aligned along the c axis yield the T dependence of the upper critical field H_{c2} shown in Fig. 7(b). One sees that $H_{c2}(T \rightarrow 0)$ is more than an order of magnitude larger than $H_c(0) = 9.5$ mT determined above, indicating that CaPd_2As_2 is a type-II superconductor. Although the demagnetization factor of the platelike crystal is large for $H \parallel c$, this has no influence on the present discussion because we only discuss the high-field behavior at the boundary with the normal state, where the magnetization is small.

For a one-band type-II BCS superconductor, the orbital critical field H_{c2}^{Orb} at $T = 0$ is given by^{66,67}

$$H_{c2}^{\text{Orb}}(0) = -A T_c \frac{dH_{c2}(T)}{dT} \Big|_{T=T_c}, \quad (28)$$

where $A = 0.73$ and 0.69 in the clean and dirty limits, respectively. From Fig. 7(b), $dH_{c2}(T)/dT|_{T=T_c} = -0.22(6)$ T/K as determined from the $\rho(T)$ data for $0.8 < T/T_c < 1.0$. Thus, for CaPd_2As_2 we estimate $H_{c2}^{\text{Orb}}(0) = 0.20(6)$ T in the clean limit and $H_{c2}^{\text{Orb}}(0) = 0.19(5)$ T in the dirty limit.

The Pauli-limiting upper critical field at $T = 0$, $H_P(0)$, is the field at which the magnetic field energy of the current carriers is equal to the superconducting condensation energy.^{68,69} Within the α -model, this is given for spectroscopic splitting factor $g = 2$ by

$$\frac{\mu_B H_P(0)}{k_B T_c} = \frac{\alpha}{\sqrt{2}} \approx 1.2473 \left(\frac{\alpha}{\alpha_{\text{BCS}}} \right), \quad (29)$$

where μ_B is the Bohr magneton and α_{BCS} is given in Eq. (20), yielding

$$H_P(0)[\text{T}] = 1.86 T_c[\text{K}] \left(\frac{\alpha}{\alpha_{\text{BCS}}} \right). \quad (30)$$

Taking $T_c = 1.27$ K, $\alpha = 1.58$ from Eq. (22), and $\alpha_{\text{BCS}} = 1.7639$ from Eq. (20) gives $H_P(0) = 2.12$ T. Since the measured $H_{c2}(0) \sim 0.15$ T $\sim 0.07 H_P(0)$ [see Fig. 7(b)], the effects of Pauli limiting on H_{c2} should be minimal. The Maki parameter α_M expresses the relative magnitudes of the orbital

and Pauli-limiting H_{c2} values as⁷⁰

$$\alpha_M = \sqrt{2} \frac{H_{c2}^{\text{Orb}}(0)}{H_P(0)}, \quad (31)$$

which gives $\alpha_M = 0.13$ for CaPd_2As_2 .

To include the influence of Pauli limiting and spin-orbit scattering of quasiparticles on H_{c2} , we analyzed the $H_{c2}(T)$ data within the Werthamer, Helfand, and Hohenberg (WHH) theory for a one-band type-II dirty-limit superconductor which calculates H_{c2} in terms of the orbital, spin-orbit scattering and Pauli spin paramagnetism contributions in dimensionless variables as⁶⁷

$$\begin{aligned}\ln \frac{1}{t} &= \sum_{\nu=-\infty}^{\infty} \left\{ \frac{1}{|2\nu+1|} - \left[|2\nu+1| + \frac{\bar{h}}{t} \right. \right. \\ &\quad \left. \left. + \frac{(\alpha_M \bar{h}/t)^2}{|2\nu+1| + (\bar{h} + \lambda_{\text{so}})/t} \right]^{-1} \right\},\end{aligned}\quad (32a)$$

where $t = T/T_c$, λ_{so} is the spin-orbit scattering parameter, and

$$\bar{h} = - \left(\frac{4}{\pi^2} \right) \frac{H_{c2}(T)/T_c}{dH_{c2}(T)/dT|_{T=T_c}}. \quad (32b)$$

WHH state that the applicability of their theory to a specific superconductor can be tested by comparing the value of α_M calculated from Eq. (31) with the value obtained from their alternative expression⁶⁷

$$\alpha_M = -0.528 \frac{dH_{c2}(T)}{dT} \Big|_{T=T_c}, \quad (33)$$

where the derivative is in units of T/K. Using our value

$$\frac{dH_{c2}(T)}{dT} \Big|_{T=T_c} = -0.22(6) \frac{\text{T}}{\text{K}} \quad (34)$$

obtained from Fig. 7(b), Eq. (33) gives $\alpha_M = 0.12(3)$, which is indeed in agreement with the above estimate $\alpha_M = 0.13$, thus indicating that the WHH theory is appropriate for fitting our $H_{c2}(T)$ data.

Reasonable agreement of our $H_{c2}(T)$ data with the WHH theory prediction for $\alpha_M = 0.13$ was obtained from Eqs. (32) with $\lambda_{\text{so}} = 0$ and $dH_{c2}(T)/dT|_{T=T_c} = -0.18$ T/K as shown in Fig. 7(b), where $H_{c2}(0) = 157$ mT. The same value of $dH_{c2}(T)/dT|_{T=T_c}$ is obtained from the dirty-limit relation⁷¹ $dH_{c2}(T)/dT|_{T=T_c} = 4.48 \times 10^4 \gamma_{\text{NV}} \rho_0$, where ρ is in units of Ω cm, indicating that CaPd_2As_2 is in the dirty limit as further documented below.

6. Ginzburg-Landau parameter

The Ginzburg-Landau parameter κ_{GL} can be estimated from the relation⁶⁰

$$\kappa_{\text{GL}} = \frac{H_{c2}}{\sqrt{2} H_c}. \quad (35)$$

Using the $T \rightarrow 0$ values $H_{c2} = 157$ mT and $H_c = 9.5$ mT gives $\kappa_{\text{GL}} = 11.7 \gg 1/\sqrt{2}$, characterizing CaPd_2As_2 as a type-II superconductor. An estimate of the lower critical field H_{c1} is then obtained from⁶⁰

$$H_{c1} = H_c \frac{\ln \kappa_{\text{GL}}}{\sqrt{2} \kappa_{\text{GL}}}, \quad (36)$$

which for $H_c(0) = 9.5$ mT and $\kappa_{GL} = 11.7$ gives $H_{c1}(0) = 1.4$ mT. Then, using the above values and the expression applicable to the high- κ_{GL} limit⁶⁰

$$\lambda_{\text{eff}}^2 = \frac{\Phi_0 H_{c2}}{4\pi H_c^2}, \quad (37)$$

where $\Phi_0 = 2.07 \times 10^{-7}$ G cm² is the flux quantum, yields the $T \rightarrow 0$ effective magnetic penetration depth $\lambda_{\text{eff}} = 530$ nm in the notation of Tinkham.

The Ginzburg-Landau coherence length at $T = 0$, $\xi(0)$, can be estimated from^{60,65}

$$H_{c2}(0) = \frac{\Phi_0}{2\pi \xi(0)^2}. \quad (38)$$

Using $H_{c2} = 157$ mT gives

$$\xi(0) = 45.8 \text{ nm}. \quad (39)$$

This $\xi(0)$ is much larger than the mean-free path $\ell = 1.52$ nm in Eq. (14) which indicates that CaPd₂As₂ is in the dirty limit.

In the dirty limit the penetration depth at $T \rightarrow 0$ is given by⁶⁰

$$\lambda_{\text{eff}}(0) = \lambda_L(0) \sqrt{1 + \frac{\xi_0}{\ell}} \quad (\text{dirty limit}). \quad (40)$$

The T dependence of ξ is given by⁶⁰

$$\frac{\xi(T)}{\xi_0} = \frac{\pi}{2\sqrt{3}} \frac{H_c(0)}{H_c(T)} \frac{\lambda_L(0)}{\lambda_{\text{eff}}(T)}, \quad (41)$$

yielding the relationship between the zero-temperature Ginzburg-Landau $\xi(0)$ and the BCS ξ_0 as

$$\frac{\xi(0)}{\xi_0} = \frac{\pi}{2\sqrt{3}} \frac{\lambda_L(0)}{\lambda_{\text{eff}}(0)}. \quad (42)$$

Combining Eqs. (40) and (42) gives

$$\frac{\xi(0)}{\xi_0} = \frac{\pi}{2\sqrt{3} \left(1 + \frac{\xi_0}{\ell}\right)} \quad (\text{dirty limit}). \quad (43)$$

Substituting the above values for $\xi(0)$ in Eq. (39) and ℓ in Eq. (14) into Eq. (43) and solving for ξ_0 gives $\xi_0 = 1690$ nm. Then, using $\lambda_L(0) = 18.6$ nm, $\xi_0 = 1690$ nm, and $\ell = 1.52$ nm, Eq. (40) gives $\lambda_{\text{eff}}(0) = 620$ nm in the dirty limit, similar to the above estimate, which is larger than the value of 210(60) nm obtained from the penetration depth measurements in Sec. VI below.

In the absence of impurity scattering, the Ginzburg-Landau parameter at $T = 0$ would have been $\kappa_{GL} = \lambda_L^{\text{calc}}(0)/\xi_0 = 18.6 \text{ nm}/1690 \text{ nm} \approx 0.01 \ll 1/\sqrt{2}$ which would have been in the extreme type-I limit instead of in the type-II regime. A similar situation was found for SrPd₂Ge₂.⁵⁹

The BCS coherence length is related to the Fermi velocity within the α -model by⁴⁶

$$\xi_0 = \frac{\hbar v_F}{\pi \Delta(0)} = \left(\frac{1}{\pi \alpha}\right) \frac{\hbar v_F}{k_B T_c}. \quad (44)$$

This allows an additional estimate of the Fermi velocity which for $\alpha = 1.58$ and $\xi_0 = 1690$ nm yields $v_F = 1.40 \times 10^8$ cm/s. This value of v_F is close to the value $v_F = 1.20 \times 10^8$ cm/s in Eq. (12) obtained from $\mathcal{D}_C(E_F)$ according to Eq. (11a), indicating the self-consistency of our modeling.

TABLE V. Measured and derived superconducting and relevant normal-state parameters for CaPd₂As₂. T_c : bulk superconducting transition temperature; γ_n : observed Sommerfeld coefficient of the linear term in the low- T normal-state heat capacity; $\lambda_{\text{el-ph}}$: electron-phonon coupling constant; ΔC_c : heat capacity jump at T_c ; $\alpha = \Delta(0)/k_B T_c$; Δ : superconducting order parameter; α_M : Maki parameter; H_c , H_p , H_{c1} , H_{c2}^{Orb} , H_{c2} : thermodynamic, Paul-limiting upper critical, lower critical, orbital upper critical, and fitted upper critical magnetic fields, respectively; κ_{GL} : Ginzburg-Landau parameter; ξ : Ginzburg-Landau coherence length; ξ_0 : BCS superconducting coherence length; ℓ : electronic mean-free path at low T ; ω_p : angular plasma frequency; λ_L : London penetration depth; λ_{eff} : magnetic penetration depth. The value of $\lambda_{\text{eff}}^{\text{obs}}(0)$ is determined from the magnetic penetration depth measurements.

CaPd ₂ As ₂ property	Value
T_c (K)	1.27(3)
γ_n (mJ/mol K ²)	6.52(2)
$\lambda_{\text{el-ph}}$ assuming $\mu^* = 0.13$	0.474
ΔC_c (mJ/mol K)	9.4(3)
$\Delta C_c/\gamma_n T_c$	1.14(3)
α (from $\Delta C_c/\gamma_n T_c$)	1.58(2)
$\Delta(0)/k_B$ (K) (observed)	2.02(14)
α_M	0.13
$H_c(T = 0)$ (mT)	9.5
H_p (T)	2.12
$H_{c1}(T = 0)$ (mT)	1.4
$H_{c2}^{\text{Orb}}(T = 0)$ (dirty limit) (T)	0.19(5)
$H_{c2}(T = 0)$ (mT)	157
κ_{GL}	11.7
$\xi(T = 0)$ (nm)	45.8
ξ_0 (nm)	1690
$\ell(m^* = m_e)$ (nm)	1.52
$\omega_p(m^* = m_e)(10^{16} \text{ rad/s})$	1.61
$\lambda_L^{\text{calc}}(0)$ (clean limit) (nm)	18.6
$\lambda_{\text{eff}}^{\text{calc}}(0)$ (dirty limit) (nm)	530–620
$\lambda_{\text{eff}}^{\text{obs}}(0)$ (nm)	210(60)

A summary of the measured and derived superconducting state parameters for CaPd₂As₂ is given in Table V.

C. Magnetization and magnetic susceptibility

Zero-field-cooled (ZFC) $\chi(T) \equiv M(T)/H$ data for a CaPd₂As₂ crystal versus T in a magnetic field $H = 3.0$ T applied along the c axis (χ_c , $H \parallel c$) and in the ab plane (χ_{ab} , $H \perp c$) are shown in Fig. 8. The data for both directions of H are strongly diamagnetic and nearly independent of T except for the Curie-like upturns at low T which were found from analysis of $M(H)$ isotherms in the Appendix to be due to the presence of a small amount of saturable paramagnetic (PM) impurities. The intrinsic $\chi(T)$ values at several temperatures obtained from the analysis of the $M(H)$ isotherms are shown by filled stars in Fig. 8, which are more accurate than the $\chi(T) = M(T)/H$ data. The χ is anisotropic with $\chi_c > \chi_{ab}$ over the entire T range.

The χ anisotropy in CaPd₂As₂ is different from the anisotropy usually observed in doped and undoped FeAs-based ThCr₂Si₂-structure compounds, where $\chi_{ab} > \chi_c$ such as in BaFe₂As₂.^{10,11} The powder and temperature average of the

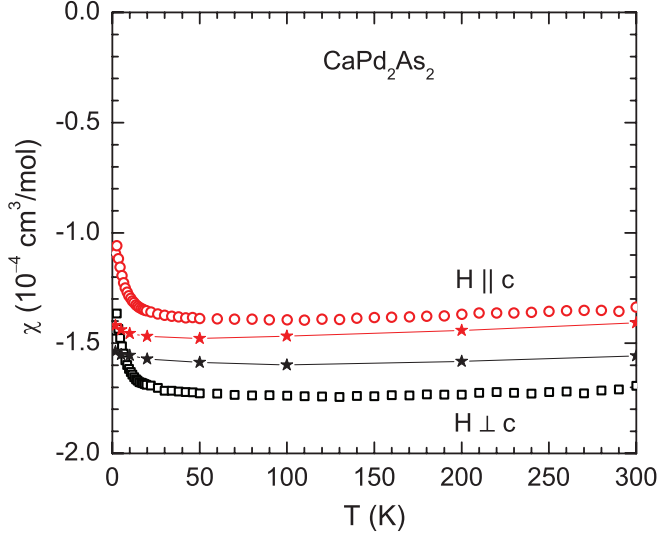


FIG. 8. (Color online) Zero-field-cooled magnetic susceptibility χ of a CaPd_2As_2 single crystal versus temperature T measured in a magnetic field $H = 3.0$ T applied along the c axis (χ_c , $H \parallel c$) and in the ab plane (χ_{ab} , $H \perp c$). The filled stars represent the intrinsic χ obtained from fitting $M(H)$ isotherm data in the Appendix by Eq. (A2a) which are more accurate than the temperature-scanned data at fixed field. The lines joining the stars are guides to the eye.

intrinsic χ obtained from fitting the $M(H)$ isotherm data in the Appendix over the T range 20 to 300 K is $\langle \chi \rangle = [2\langle \chi_{ab} \rangle + \langle \chi_c \rangle]/3 = -1.5 \times 10^{-4} \text{ cm}^3/\text{mol}$.

The diamagnetic susceptibilities in Fig. 8 seem to be rather large. For the purpose of comparing the diamagnetic susceptibilities of different materials, a comparison of the thermodynamic dimensionless magnetic susceptibility per unit volume χ_V (volume susceptibility) is most appropriate. Using the molar volume $V_M = 55.7 \text{ cm}^3/\text{mol}$ for CaPd_2As_2 in Table I and $\chi_{ab}(100 \text{ K}) = -1.6 \times 10^{-4} \text{ cm}^3/\text{mol}$ from Fig. 8 (black star), one obtains $\chi_{Vab} = \chi_{ab}/V_M$ in the ab plane as

$$\chi_{Vab}(100 \text{ K}) = -0.29 \times 10^{-5} \quad (\text{CaPd}_2\text{As}_2). \quad (45)$$

This value can be compared with the respective values for elemental Bi and C (graphite) that are well known for their exceptionally strong diamagnetism. Bi has a rhombohedral crystal structure with a mass density $\rho_m = 9.8 \text{ g/cm}^3$ and a gram susceptibility in the hexagonal ab plane $\chi_{gab}(100 \text{ K}) = -1.9 \times 10^{-6} \text{ cm}^3/\text{g}$.⁷² The volume susceptibility $\chi_V = \rho_m \chi_g$ is then

$$\chi_{Vab}(100 \text{ K}) = -1.9 \times 10^{-5} \quad (\text{Bi}). \quad (46)$$

On the other hand, using $\rho_m = 2.27 \text{ g/cm}^3$ for hexagonal highly oriented pyrolytic graphite (HOPG) and $\chi_{gc}(100 \text{ K}) = -2.3 \times 10^{-5} \text{ cm}^3/\text{g}$,⁷³ one obtains

$$\chi_{Vc}(100 \text{ K}) = -5.2 \times 10^{-5} \quad (\text{C, HOPG}). \quad (47)$$

These values for Bi and graphite are about 6.5 and 18 times more diamagnetic than the value for CaPd_2As_2 in Eq. (45), respectively. However, these three values are all much less diamagnetic than the value $\chi_V = -1/4\pi \approx -0.0796$ for the diamagnetic susceptibility of a superconductor at low fields with zero demagnetization factor due to complete exclusion

of the magnetic induction from the interior (except within a magnetic field penetration depth of the surface).

The different contributions to the intrinsic χ are

$$\chi = \chi_{\text{core}} + \chi_{\text{VV}} + \chi_L + \chi_P, \quad (48)$$

where the first three terms are orbital susceptibilities and the last term is the Pauli spin susceptibility of the conduction carriers. χ_{core} is the isotropic diamagnetic susceptibility of localized core electrons, χ_{VV} is the generally anisotropic paramagnetic Van Vleck susceptibility, and χ_L is the generally isotropic Landau diamagnetic susceptibility of the conduction carriers.

The χ_{core} is estimated using atomic diamagnetic susceptibilities⁷⁴ which gives $\chi_{\text{core}} = -1.78 \times 10^{-4} \text{ cm}^3/\text{mol}$. The χ_P is related to $\mathcal{D}(E_F)$ by^{11,75}

$$\chi_P = \frac{g^2}{4} \mu_B^2 \mathcal{D}_{\text{band}}(E_F), \quad (49)$$

where we assume that there are no many-body enhancements to χ_P . Then, using $g = 2$ and $\mathcal{D}(E_F) = 1.87 \text{ states/eV f.u.}$ for both spin directions, from Table IV we obtain $\chi_P = 6.0 \times 10^{-5} \text{ cm}^3/\text{mol}$. The χ_L is related to χ_P by^{75,76}

$$\chi_L = -\frac{1}{3} \left(\frac{m_e}{m_{\text{band}}^*} \right)^2 \chi_P, \quad (50)$$

where we assume that χ_L is not enhanced by the electron-phonon interaction. Assuming $m_{\text{band}}^* = m_e$ we obtain $\chi_L = -2.0 \times 10^{-5} \text{ cm}^3/\text{mol}$ from the above value of χ_P . Then, χ_{VV} is obtained by subtracting these three contributions from the measured χ according to Eq. (48). The four contributions to the intrinsic χ are summarized in Table VI, along with corresponding values for SrPd_2As_2 and BaPd_2As_2 determined below.

It is seen in Table VI that the inferred value of χ_{VV} for CaPd_2As_2 is negative, which is unphysical. The reason for this error is not clear. The most likely source of the negative χ_{VV} value is a small error in correcting the total measured magnetic moment for the sample holder contribution, which was up to 40% of the total measured moment. Thus, the uncertainty in the measured χ values is of order 10% as discussed in Sec. II. In particular, the negative χ_{VV} is about 8% of the measured moment, and an error of only 4% in the sample holder correction could cause the derived χ_{VV} to be negative.

TABLE VI. Estimated contributions to the intrinsic angle- and temperature-averaged magnetic susceptibilities $\langle \chi \rangle$ of APd_2As_2 ($A = \text{Ba, Ca, Sr}$) crystals. Here χ_P is the Pauli spin susceptibility of the conduction carriers, and the orbital susceptibility contributions are the diamagnetism χ_{core} of the atomic electron cores, the Landau diamagnetism χ_L of the conduction carriers, and the Van Vleck paramagnetism χ_{VV} . All susceptibilities are in units of $10^{-5} \text{ cm}^3/\text{mol}$. Possible reasons for the unphysical negative value of $\langle \chi_{\text{VV}} \rangle$ for CaPd_2As_2 are discussed in the text.

Compound	$\langle \chi \rangle$	χ_{core}	χ_P	χ_L	$\langle \chi_{\text{VV}} \rangle$
CaPd_2As_2	-15.4	-17.8	6.0	-2.0	-1.6
SrPd_2As_2	-3.9	-19.3	6.0	-2.0	11.4
BaPd_2As_2	-12.4	-21.6	6.6	-2.2	4.8

V. PHYSICAL PROPERTIES OF SrPd_2As_2 CRYSTALS

A. Electrical resistivity

The in-plane $\rho(T)$ data for SrPd_2As_2 measured on two different crystals #1 and #2 at different H are shown in Fig. 9. Metallic behavior is evident from the T dependence of ρ in Fig. 9(a). The expanded plot of $\rho(T)$ in Fig. 9(b) reveals a superconducting transition at $T_c = 1.5(1)$ K. The T_c is suppressed with increasing H , as shown. The data in Fig. 9(b) are noisy due to the small sample size and the small voltage signal arising from the small magnitude of the resistivity at low T .

The two crystals were found to have different residual resistivities and RRR values. For crystal #1, $\rho_0(1.8 \text{ K}) =$

$7.5 \mu\Omega \text{ cm}$ and $\text{RRR} = \rho(300 \text{ K})/\rho(1.8 \text{ K}) \approx 8$, whereas for crystal #2, $\rho_0 = 4.9 \mu\Omega \text{ cm}$ and $\text{RRR} \approx 4$. The reason the room temperature resistivities of the two crystals are different (≈ 60 and $20 \mu\Omega \text{ cm}$, respectively) is unknown. Since crystal #1 has the higher RRR, we analyzed the $\rho(T)$ data of this crystal in Fig. 9(a) using the BG model. A fit of the $\rho(T)$ data in Fig. 9(a) by Eqs. (2) for $1.8 \text{ K} \leq T \leq 300 \text{ K}$ gives $\rho_0 = 7.57(6) \mu\Omega \text{ cm}$, $\rho(\Theta_R) = 27.6(5) \mu\Omega \text{ cm}$, and $\Theta_R = 170(3) \text{ K}$, where we used our analytic Padé approximant⁵⁴ in place of the integral in Eq. (2a). The good fit obtained is shown by the red curve in Fig. 9(a). The value of \mathcal{R} obtained from the value of $\rho(\Theta_R)$ using Eq. (2b) is $\mathcal{R} = 29.2 \mu\Omega \text{ cm}$. The parameters obtained from the fit are summarized in Table III.

B. Heat capacity

The $C_p(T)$ data for SrPd_2As_2 are shown in Fig. 10. The $C_p(T = 300 \text{ K}) \approx 124 \text{ J/mol K}$ is close to the classical Dulong-Petit high- T limit $C_V = 5R = 124.7 \text{ J/mol K}$. In order to correlate low- T $C_p(T)$ data with $\rho(T)$ data obtained on the same crystal, we also measured the low- T $C_p(T)$ on a different crystal #2 as shown in Fig. 11(a), for which the $\rho(T)$ data are shown in Fig. 9(b). As shown in the inset of Fig. 10, a rather sharp heat capacity jump is observed at $T_c = 0.92(5) \text{ K}$ due to the superconducting transition, where we define T_c to be the transition midpoint. Two important differences are observed between the $C_p(T)$ and $\rho(T)$ data on crystal #2. First, the T_c obtained from the two measurements are different: $T_c = 0.92(5) \text{ K}$ from $C_p(T)$ and $T_c = 1.5(1) \text{ K}$ from $\rho(T)$. Second, while the superconductivity is suppressed to a temperature below 0.45 K by $H = 0.05 \text{ T}$ in $C_p(T)$, superconductivity occurs at $\approx 1 \text{ K}$ even at $H = 0.15 \text{ T}$ in $\rho(T)$.

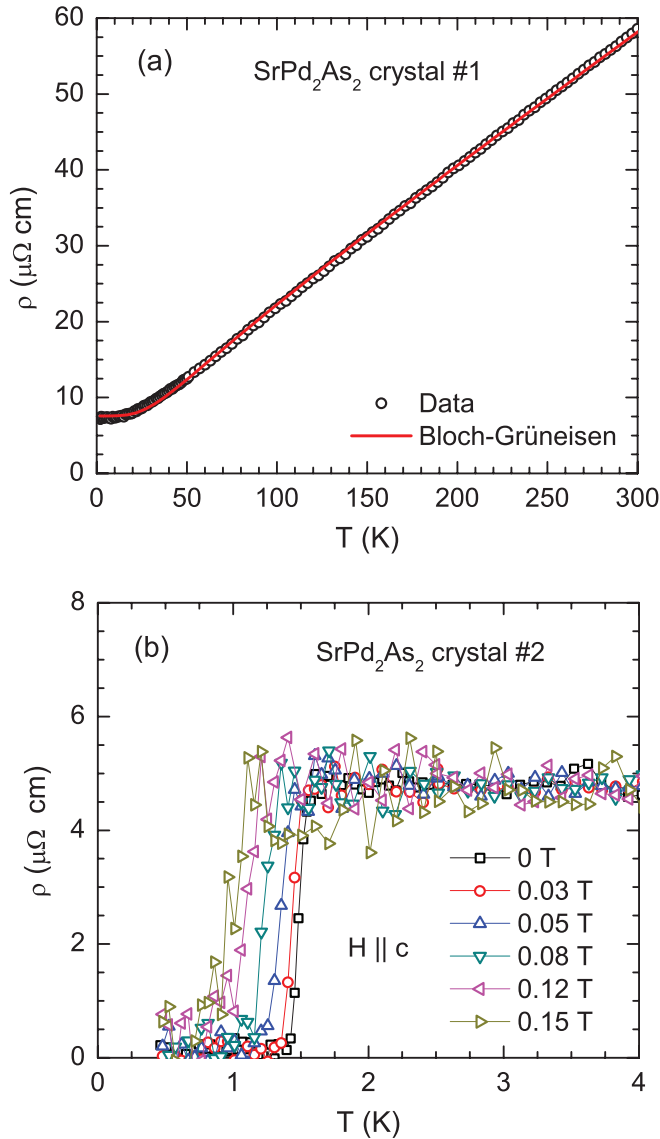


FIG. 9. (Color online) (a) In-plane electrical resistivity ρ of a SrPd_2As_2 crystal (crystal #1) versus temperature T measured in applied magnetic field $H = 0$. The red curve is a fit by the Bloch-Grüneisen model in Eqs. (2). (b) Expanded plot of the low- T $\rho(T)$ data for SrPd_2As_2 crystal #2 for $0.45 \text{ K} \leq T \leq 4 \text{ K}$ showing the superconducting transition for different H applied along the c axis. The noise in the data is due to the small size of the crystal and the small magnitude of ρ at low temperatures.

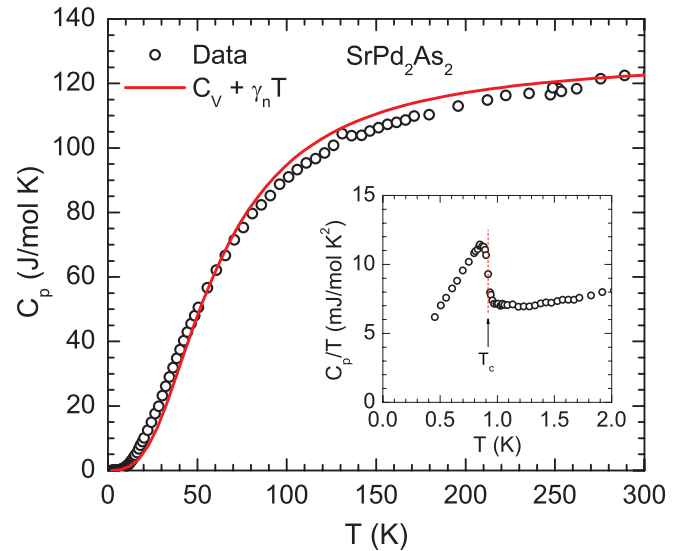


FIG. 10. (Color online) The heat capacity C_p of a SrPd_2As_2 single crystal versus temperature T measured in zero magnetic field H . The red curve is the fitted sum of the contributions from the Debye lattice heat capacity $C_{V\text{Debye}}(T)$ and predetermined electronic heat capacity $\gamma_n T$ according to Eq. (5a). Inset: Expanded plot of C_p/T versus T for $0.45 \text{ K} \leq T \leq 2.0 \text{ K}$ measured on a different crystal (crystal #2 of Fig. 9) at field $H = 0$. The vertical dotted red line indicates the T_c .

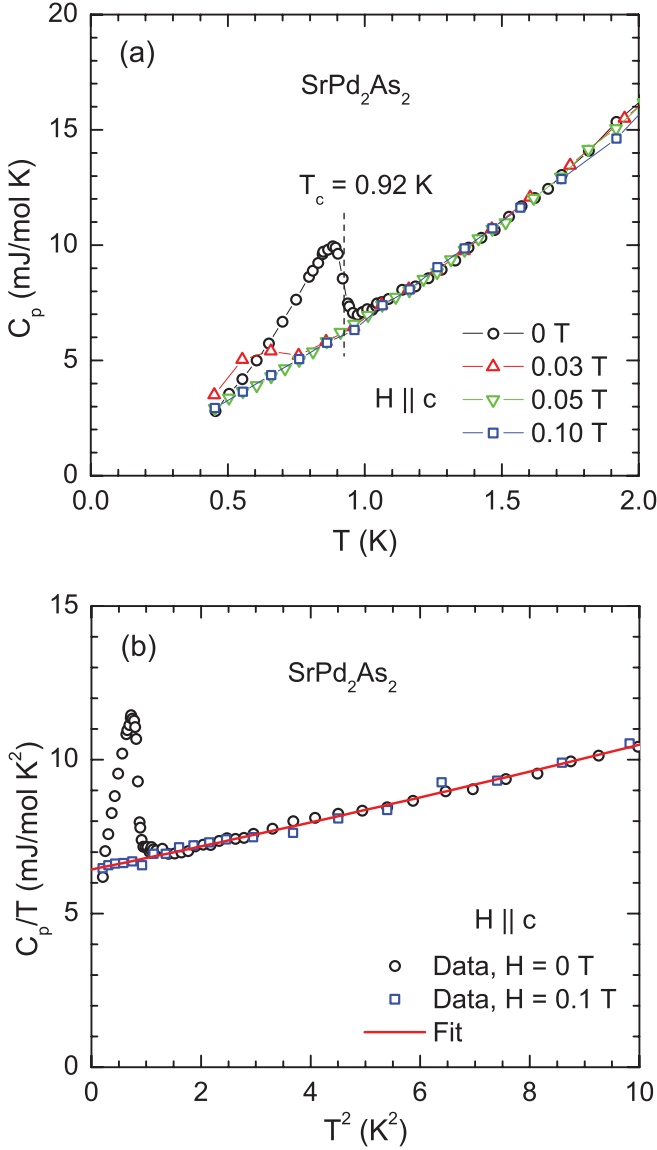


FIG. 11. (Color online) (a) Heat capacity C_p versus temperature T of a SrPd_2As_2 single crystal (crystal #2 of Fig. 9) for $0.45 \text{ K} \leq T \leq 2.0 \text{ K}$ measured at the indicated values of applied magnetic field H with $H \parallel c$. (b) C_p/T vs T^2 for $0.45 \text{ K} \leq T \leq 3.2 \text{ K}$ with $H = 0$ and 0.1 T . The red curve is a fit of the $H = 0.1 \text{ T}$ data for $0.45 \text{ K} \leq T \leq 4.4 \text{ K}$ and the $H = 0$ data for $1.3 \text{ K} \leq T \leq 4.4 \text{ K}$ by Eq. (3) (the fitted data from 3.2 to 4.4 K are not shown).

These two observations suggest the presence of filamentary superconductivity in SrPd_2As_2 which is probed by $\rho(T)$ at temperatures above the bulk T_c whereas $C_p(T)$ measures the bulk superconductivity.

A fit of the normal-state $C_p(T)/T$ versus T^2 data using the $H = 0.1 \text{ T}$ data for $0.45 \text{ K} \leq T \leq 4.4 \text{ K}$ and the $H = 0$ data for $1.3 \text{ K} \leq T \leq 4.4 \text{ K}$ in Fig. 11(b) by Eq. (3) (the fitted data from 3.2 to 4.4 K are not shown) gives $\gamma_n = 6.43(3) \text{ mJ/mol K}^2$, $\beta = 0.369(8) \text{ mJ/mol K}^4$, and $\delta = 3.7(5) \mu\text{J/mol K}^6$ as shown by the red curve. The Debye temperature estimated from β using Eq. (4) is $\Theta_D = 298(3) \text{ K}$. A fit of $C_p(T)$ in Fig. 10 over the entire T range (2 – 300 K) by Eqs. (5) with γ_n fixed to the above value and using the

Padé approximant⁵⁴ in place of the Debye function gives $\Theta_D = 245(3) \text{ K}$. The fit is shown by the red curve in Fig. 10. The value of Θ_D is smaller than the value of $298(3) \text{ K}$ obtained from the low- T fit, indicating a T -dependent Θ_D .⁵⁴ The parameters obtained from the analyses of the normal-state $C_p(T)$ data are summarized in Table IV.

The electron-phonon coupling constant is estimated from Eq. (9) as $\lambda_{\text{el-ph}} = 0.443$ using $\mu^* = 0.13$, $T_c = 0.92 \text{ K}$, and $\Theta_D = 298 \text{ K}$. Then we estimate $\mathcal{D}_C(E_F) = 2.73(2) \text{ states/(eV f.u.)}$ for both spin directions from Eq. (6) and $\mathcal{D}_{\text{band}}(E_F) = 1.89(1) \text{ states/(eV f.u.)}$ for both spin directions from Eq. (8a), which is very close to that of CaPd_2As_2 in Table IV. The Fermi velocity obtained from Eq. (11a) is $v_F = 1.17 \times 10^8 \text{ cm/s}$, and the mean-free path for this value of v_F and $\rho_0 = 4.9 \mu\Omega \text{ cm}$ using Eq. (13) is $\ell = 11.6 \text{ nm}$. The ω_p and $\lambda_L(0)$ estimated from Eqs. (16) and (18), respectively, are listed in Table VII.

The electronic contribution $C_e(T)$ to the measured low- T $C_p(T)$ of SrPd_2As_2 , obtained by subtracting $\beta T^3 + \delta T^5$ from $C_p(T)$ according to Eq. (3), is plotted versus T in Fig. 12(a), and $C_e(T)/T$ is plotted versus T in Fig. 12(b). Utilizing the entropy-conserving construction in Fig. 12(b) we obtain $\Delta C_e(T_c)/T_c = 5.0(2) \text{ mJ/mol K}^2$,

TABLE VII. Measured and derived superconducting and relevant normal-state parameters for SrPd_2As_2 . T_c : bulk superconducting transition temperature; γ_n : observed Sommerfeld coefficient of the linear term in the low- T normal-state heat capacity; $\lambda_{\text{el-ph}}$: electron-phonon coupling constant; ℓ : mean-free path at low T ; ω_p : plasma angular frequency; λ_L : London penetration depth; λ_{eff} : magnetic penetration depth; H_{c2}^{Orb} : orbital upper critical magnetic field; Δ : superconducting order parameter; $\alpha = \Delta(0)/k_B T_c$; ΔC_e : heat capacity jump at T_c ; H_P : Pauli-limiting upper critical field; α_M : Maki parameter; H_c , H_{c1} , H_{c2} : thermodynamic, lower critical, and fitted upper critical magnetic fields, respectively; κ_{GL} : Ginzburg-Landau parameter; ξ : Ginzburg-Landau coherence length; ξ_0 : BCS superconducting coherence length.

SrPd_2As_2 property	Value	
T_c (K)	0.92(5)	
γ_n (mJ/mol K ²)	6.43(3)	
$\lambda_{\text{el-ph}}$	0.443	
$\ell(m^* = m_e)$ (nm)	11.6	
$\omega_p(m^* = m_e)$ (10 ¹⁶ rad/s)	1.52	
$\lambda_L^{\text{calc}}(0)$ (clean limit) (nm)	19.7	
$\lambda_{\text{eff}}^{\text{obs}}(0)$ (nm)	170(70)	
$H_{c2}^{\text{Orb}}(T = 0)$ (dirty limit) (T)	0.073	
$\Delta(0)/k_B$ (K) (observed)	2.05(20)	
	$\alpha = 1.30$	$\alpha = 1.50$
ΔC_e (mJ/mol K)	4.6(2)	6.1(4)
$\Delta C_e/\gamma_n T_c$	0.77(5)	1.03(8)
$H_P(0)$ (T)	1.37	1.58
α_M	0.08	0.07
$H_c(T = 0)$ (mT)	5.5	6.3
$H_{c1}(T = 0)$ (mT)	0.94	1.17
$H_{c2}(T = 0)$ (mT)	70	70
κ_{GL}	9.0	7.8
$\xi(T = 0)$ (nm)	69	69
ξ_0 (nm)	509	509
$\lambda_{\text{eff}}^{\text{calc}}(0)$ (dirty limit) (nm)	130	130

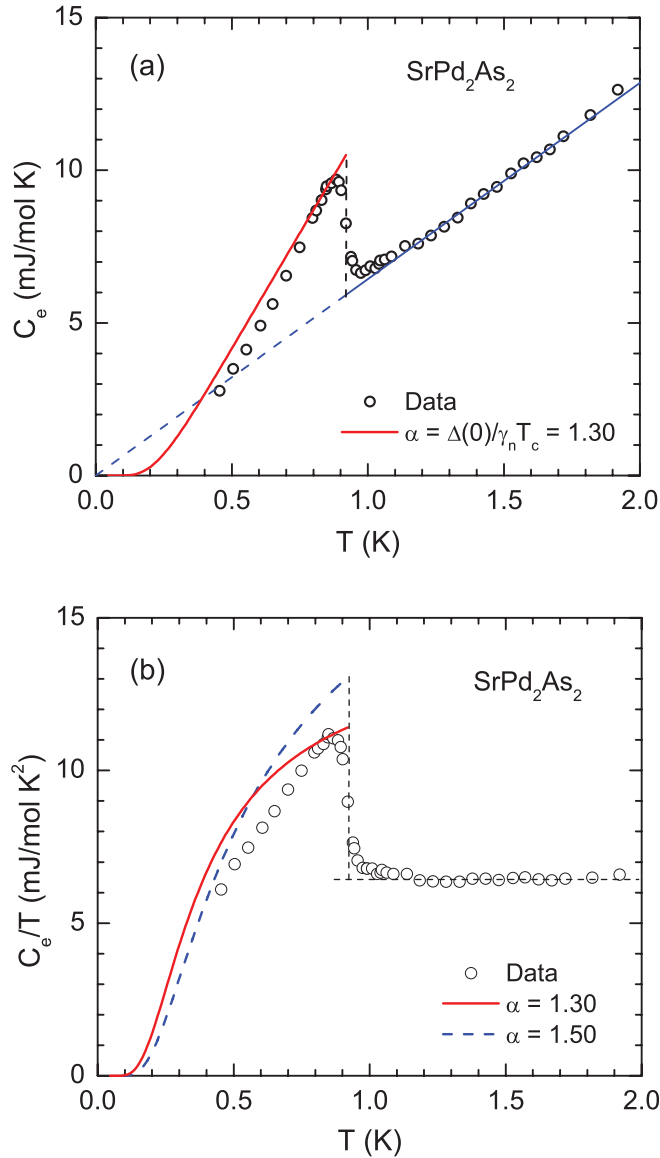


FIG. 12. (Color online) (a) The electronic contribution C_e versus temperature T at low T obtained by subtracting the phonon contribution from the measured $C_p(T)$ of SrPd₂As₂. (b) C_e/T versus T . The solid red curves in (a) and (b) are the theoretical predictions of the α -model for $\alpha = 1.30$ and the dashed blue curve in (b) is for $\alpha = 1.50$.

$\Delta C_e(T_c) = 4.6(2)$ mJ/mol K using $T_c = 0.92(5)$ K, and $\Delta C_e(T_c)/\gamma_n T_c = 0.77(5)$ using $\gamma_n = 6.43(3)$ mJ/mol K². The value of $\Delta C_e(T_c)/\gamma_n T_c$ is significantly smaller than the BCS weak-coupling value of 1.43, as was also the case for CaPd₂As₂ discussed above, and from Eq. (21) we obtain $\alpha = 1.30(4)$ which may be compared with the BCS value of 1.764. In Figs. 12(a) and 12(b) we show as the red curves the respective theoretical predictions of the α -model obtained using $\alpha = 1.30$ in Eqs. (23). Also shown as the dashed blue curve in Fig. 12(b) is the theoretical prediction for $\alpha = 1.50$, which is the value that best fits the $H_c(T)$ data in Fig. 13(a) below.

The $H_c(T)$ for SrPd₂As₂ is obtained by integrating the $C_e(T)$ data in Fig. 12 according to Eqs. (24) and the results are shown in Fig. 13(a). The shoulder just above T_c arises

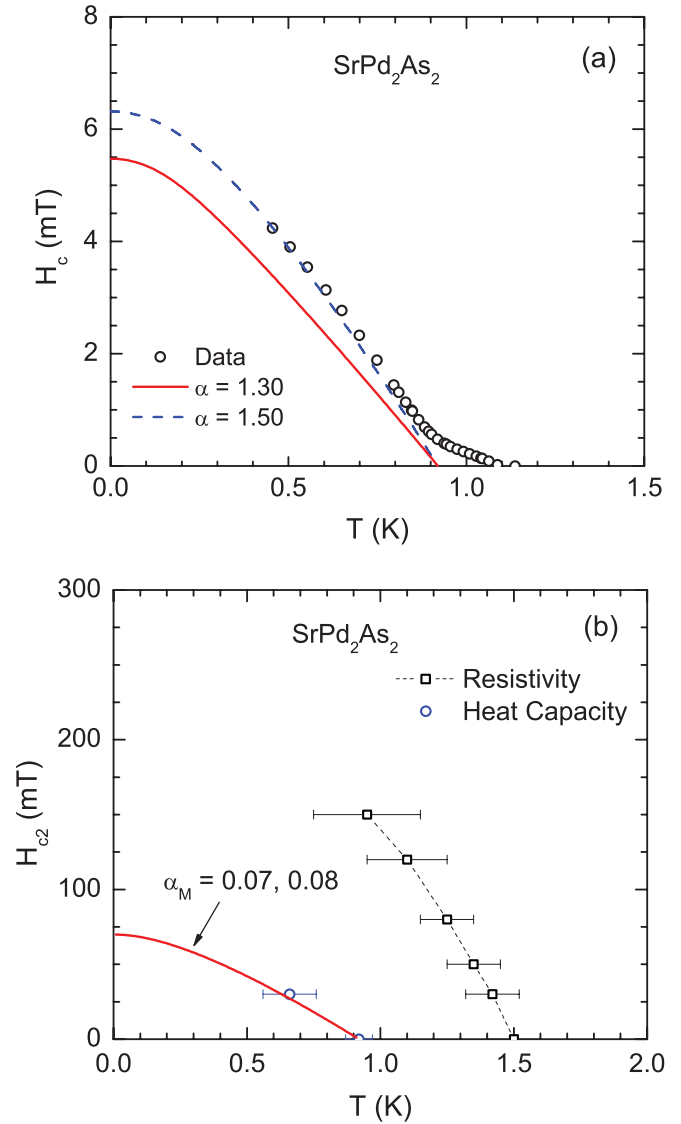


FIG. 13. (Color online) (a) Thermodynamic critical field $H_c(T)$ obtained from a double integration of the zero-field superconducting state $C_p(T)$ data according to Eqs. (24). The solid red and dashed blue curves are the theoretical predictions of the α -model for $\alpha = 1.30$ and 1.50, respectively. (b) Upper critical field $H_{c2}(T)$ of SrPd₂As₂ determined from the electrical resistivity $\rho(T, H)$ and heat capacity $C_p(T, H)$ data in Figs. 9(b) and 10(b), respectively. The red curve is the prediction of the WHH theory in Eqs. (32) for $\alpha_M = 0.07$ and 0.08 and $\lambda_{so} = 0$.

from the high- T shoulder in the $C_e(T)$ data in Figs. 12(a) and 12(b). The value of $H_c(0)$ is calculated from Eq. (26) using $\alpha = 1.30$, $\gamma_n = 6.43$ mJ/mol K², and $T_c = 0.92$ K, yielding $H_c(0) = 5.5$ mT. The theoretical prediction of the α -model in Eqs. (27) for $H_c(T)$ using these parameters is plotted in Fig. 13(a). Although the T dependence of the data is reproduced, the calculated magnitude does not agree with the data. A better fit as shown in Fig. 13(a) by the blue dashed curve is obtained using $\alpha = 1.50$, for which $H_c(0)$ is calculated as above to be 6.3 mT.

The H_{c2} versus T data obtained from the above $C_p(T)$ and $\rho(T)$ measurements with $H \parallel c$ are shown in Fig. 13(b).

As already mentioned the two measurements show different T_c 's in zero field. Consistent with this difference, the $H_{c2}(T)$ behavior derived from the $\rho(T)$ data indicates that the upper critical field of the filamentary superconductivity is larger than the bulk H_{c2} . The above values of $H_c(0)$ for both $\alpha = 1.30$ or 1.50 are much smaller than the bulk $H_{c2}(0)$ extrapolated from the heat capacity data in Fig. 13(b), indicating type-II superconductivity in SrPd_2As_2 as was also found above to be the case in CaPd_2As_2 .

From the $C_p(T)$ data in Fig. 13(b) one obtains $dH_{c2}(T)/dT|_{T=T_c} = -0.12(4)$ T/K. Equation (28) then gives $H_{c2}^{\text{Orb}}(0) = 0.077$ T in the clean limit and $H_{c2}^{\text{Orb}}(0) = 0.073$ T in the dirty limit. Using $\alpha = 1.30$, the Pauli-limiting field is obtained from Eq. (30) as $H_P(0) = 1.37$ T and the Maki parameter in Eq. (31) is then $\alpha_M = 0.08$. An estimate of $H_{c2}(T)$ obtained from the WHH prediction in Eqs. (32) using $\alpha_M = 0.08$ and $\lambda_{\text{so}} = 0$ is shown as the solid red curve in Fig. 13(b), from which we obtain $H_{c2}(0) = 70$ mT.

The Ginzburg-Landau parameter is obtained from Eq. (35) using $H_{c2}(0) = 70$ mT and $H_c(0) = 5.5$ mT, yielding $\kappa_{\text{GL}} = 9.0$. The lower critical field estimated from Eq. (36) is $H_{c1}(0) = 0.94$ mT. The Ginzburg-Landau coherence length at $T = 0$ obtained from Eq. (38) is $\xi(0) = 69$ nm which together with $\ell = 11.6$ nm and Eq. (41) for the dirty limit gives $\xi_0 = 509$ nm. The Fermi velocity estimated from ξ_0 using Eq. (44) is $v_F = 0.25 \times 10^8$ cm/s for $\alpha = 1.30$ which is of the same order as the above estimated value of v_F from the density of states. Corresponding values of the above parameters for $\alpha = 1.50$ were also calculated. A summary of the measured and derived superconducting parameters for SrPd_2As_2 is given in Table VII.

C. Magnetization and magnetic susceptibility

The ZFC $\chi(T) \equiv M(T)/H$ data for a SrPd_2As_2 single crystal measured in $H = 3.0$ T are shown in Fig. 14 together with the intrinsic χ obtained from fitting $M(H)$ isotherm data for $H \geq 2$ T in the Appendix by Eq. (A1). These two data sets are in excellent agreement over the whole T range, indicating the near absence of ferromagnetic and saturable paramagnetic impurities in the crystal. The very small upturns below ~ 10 K in $\chi(T)$ in Fig. 14 are attributed to a trace amount of paramagnetic impurities. The χ is diamagnetic and exhibits a weak T dependence with a strong anisotropy $\chi_{ab} > \chi_c$. The large anisotropy in χ most likely originates from anisotropy in the paramagnetic Van Vleck orbital contribution χ_{VV} in Eq. (48), although the strong temperature dependence of the anisotropy is unusual and unexpected for such a compound and for which the origin is not clear. Despite having the same crystal structure, the χ anisotropy in SrPd_2As_2 is opposite to that of CaPd_2As_2 in Fig. 8 for which we observed $\chi_{ab} < \chi_c$. This difference in the sign of the anisotropy between the two compounds is evidently again attributable to a difference in the sign of the anisotropy in the Van Vleck contributions between the two compounds.

The powder and temperature (1.8–300 K) average of the intrinsic χ obtained from the $M(H)$ isotherms in the Appendix is $\langle \chi \rangle = -3.9 \times 10^{-5}$ cm³/mol. The diamagnetic core susceptibility estimated using the atomic diamagnetic susceptibilities⁷⁴ is $\chi_{\text{core}} = -1.93 \times 10^{-4}$ cm³/mol. The Pauli

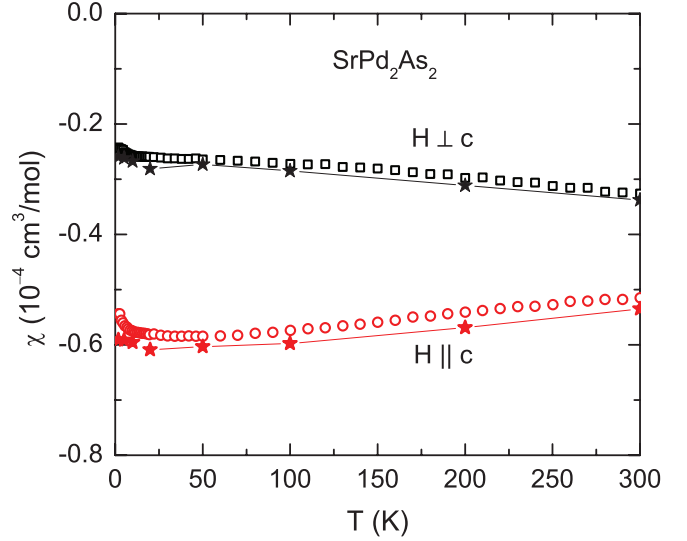


FIG. 14. (Color online) Zero-field-cooled magnetic susceptibility χ of a SrPd_2As_2 single crystal versus temperature T in a magnetic field $H = 3.0$ T applied along the c axis (χ_c , $H \parallel c$) and in the ab plane (χ_{ab} , $H \perp c$). The filled stars represent the intrinsic χ obtained in the Appendix from fitting $M(H)$ isotherm data by Eq. (A1). The lines joining the stars are guides to the eye.

susceptibility estimated from Eq. (49) using $\mathcal{D}_{\text{band}}(E_F) = 1.89$ states/eV f.u. for both spin directions is $\chi_P = 6.1 \times 10^{-5}$ cm³/mol. The $\chi_L = -2.0 \times 10^{-5}$ cm³/mol was obtained by taking $m_{\text{band}}^* = m_e$ in Eq. (50). Then $\langle \chi_{\text{VV}} \rangle$ is obtained from these values using Eq. (48). The various χ contributions are summarized in Table VI.

VI. MAGNETIC PENETRATION DEPTH MEASUREMENTS OF CaPd_2As_2 AND SrPd_2As_2

Figure 15 shows the temperature variation of the ab -plane magnetic penetration depth $\Delta\lambda_{\text{eff}}(T) \equiv \lambda_{\text{eff}}(T) - \lambda_{\text{eff}}(0)$ measured in CaPd_2As_2 and SrPd_2As_2 crystals, represented by open circles and triangles, respectively. The absolute value of the penetration depth was obtained using the TDR technique by matching the frequency shift $\Delta f(T)$ to the skin depth δ calculated from the resistivity. The superconducting transition temperature was determined as the temperature of the maximum of $d\Delta\lambda_{\text{eff}}/dT$. The determined T_c 's are 1.34 and 1.26 K for CaPd_2As_2 and SrPd_2As_2 , respectively. These values are higher than the bulk T_c 's of 1.27(3) and 0.92(5) K determined from respective $C_p(T)$ data (Tables V and VII, respectively). Even so, the actual onset of the diamagnetic response is observed at even higher temperatures $T_c^{\text{onset}} = 1.50$ and 1.72 K for CaPd_2As_2 and SrPd_2As_2 , respectively. The T dependencies of $\Delta\lambda_{\text{eff}}$ for the two compounds up to T_c are shown in the inset of Fig. 15.

At low temperatures, the $\Delta\lambda_{\text{eff}}(T)$ in Fig. 15 of each sample shows a clear saturation on cooling, which is an indication of a fully gapped superconducting order parameter in both compounds. Our compounds are dirty-limit superconductors, for which the magnetic penetration depth in the single-band

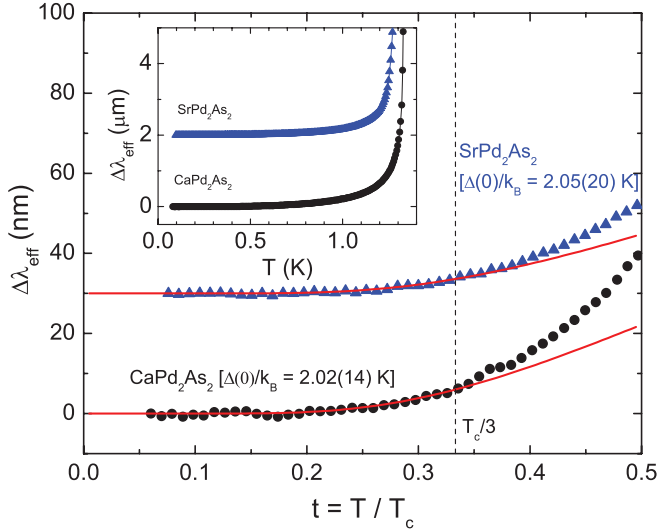


FIG. 15. (Color online) The change $\Delta\lambda_{\text{eff}} \equiv \lambda_{\text{eff}}(T) - \lambda_{\text{eff}}(T \rightarrow 0)$ of the magnetic penetration depth λ_{eff} measured in CaPd_2As_2 (filled circles) and SrPd_2As_2 (filled triangles). The data for SrPd_2As_2 are shifted vertically upwards by 30 nm for clarity. The solid curve for each compound is the best fit of the data by the prediction in Eq. (52) for a single-gap s -wave BCS superconductor for $T \lesssim T_c/3$. The vertical dashed line is the upper temperature limit for the fits. Inset: $\Delta\lambda_{\text{eff}}(T)$ for both compounds up to $T = T_c$. The data for SrPd_2As_2 are all shifted upwards by 2 μm for clarity.

model for $T/T_c \ll 1$ in Tinkham's notation⁶⁰ is

$$\lambda_{\text{eff}}(T) = \lambda_L(T) \sqrt{1 + \frac{\xi_0}{\ell}}, \quad (51a)$$

where $\lambda_L(T)$ is the clean-limit BCS London penetration depth prediction, yielding the $T = 0$ expression in Eq. (40), and also for $T/T_c \ll 1$ the expression

$$\frac{\lambda_{\text{eff}}(T)}{\lambda_{\text{eff}}(0)} = \frac{\lambda_L(T)}{\lambda_L(0)}. \quad (51b)$$

Defining $\Delta\lambda(T) = \lambda(T) - \lambda(0)$, one obtains

$$\frac{\Delta\lambda_{\text{eff}}(T)}{\lambda_{\text{eff}}(0)} = \frac{\Delta\lambda_L(T)}{\lambda_L(0)}. \quad (51c)$$

The right-hand side of this equation is just the clean-limit BCS prediction for local electrodynamics given by^{46,49,62}

$$\frac{\Delta\lambda_L(T)}{\lambda_L(0)} = \sqrt{\frac{\pi \Delta(0)}{2k_B T}} \exp\left[-\frac{\Delta(0)}{k_B T}\right]. \quad (52)$$

Combining Eqs. (51c) and (52) gives

$$\Delta\lambda_{\text{eff}}(T) = \lambda_{\text{eff}}(0) \sqrt{\frac{\pi \Delta(0)}{2k_B T}} \exp\left[-\frac{\Delta(0)}{k_B T}\right]. \quad (53)$$

The experimental data are fitted well up to $T \approx T_c/3$ by Eq. (53) as shown by the solid curves in Fig. 15, where the fitting parameters are $\lambda_{\text{eff}}(0) = 210 \pm 60$ nm and $\Delta(0)/k_B = 2.02 \pm 0.14$ K for CaPd_2As_2 and $\lambda_{\text{eff}}(0) = 170 \pm 70$ nm and $\Delta(0)/k_B = 2.05 \pm 0.20$ K for SrPd_2As_2 . The listed errors are systematic errors obtained from the spread of the fitting parameters depending on different choices of the upper temperature limit near $T_c/3$.

Using the bulk T_c values in Tables V and VII and the above values of $\Delta(0)/k_B$, we obtain $\alpha = 1.59(14)$ for CaPd_2As_2 and $\alpha = 2.23(0.32)$ for SrPd_2As_2 . The value of α for CaPd_2As_2 is identical within the error bars to the value of 1.58(2) in Eq. (22) that was determined from the heat capacity jump, both of which are smaller than the value $\alpha_{\text{BCS}} \approx 1.764$ expected for an isotropic weak-coupling BCS superconductor.^{46,62} This reduction is most likely due to a moderate anisotropy of the order parameter⁴⁶ rather than multiple order parameters because well-known multigap superconductors such as MgB_2 ,⁷⁷ NbSe_2 ,⁷⁸ and LiFeAs (Ref. 79) have shown much lower values of α for the smaller gap. The accuracy of α for SrPd_2As_2 is uncertain because of the significantly larger superconducting transition width obtained from the heat capacity measurements for this compound, and will therefore not be further considered.

The above parameter values obtained for CaPd_2As_2 and SrPd_2As_2 are listed in Tables V and VII, respectively.

VII. PHYSICAL PROPERTIES OF BaPd_2As_2 CRYSTALS

A. Electrical resistivity

The in-plane $\rho(T)$ data for a BaPd_2As_2 crystal are shown in Fig. 16. The T dependence of ρ reveals metallic behavior with a very small residual resistivity $\rho_0 \approx 1 \mu\Omega \text{ cm}$ and a large RRR ≈ 25 , demonstrating the high quality of the crystal. The scale of the resistivity for BaPd_2As_2 is smaller and the RRR is much larger than those of CaPd_2As_2 and SrPd_2As_2 . The $\rho(T)$ data were fitted by Eqs. (2) for $2 \text{ K} \leq T \leq 300 \text{ K}$ using the analytic Padé approximant function⁵⁴ as shown by red curve in Fig. 16. The excellent fit obtained yielded the fitting parameters $\rho_0 = 1.02(1) \mu\Omega \text{ cm}$, $\rho(\Theta_R) = 8.84(1) \mu\Omega \text{ cm}$, and $\Theta_R = 114(1) \text{ K}$. The value of the constant \mathcal{R} obtained

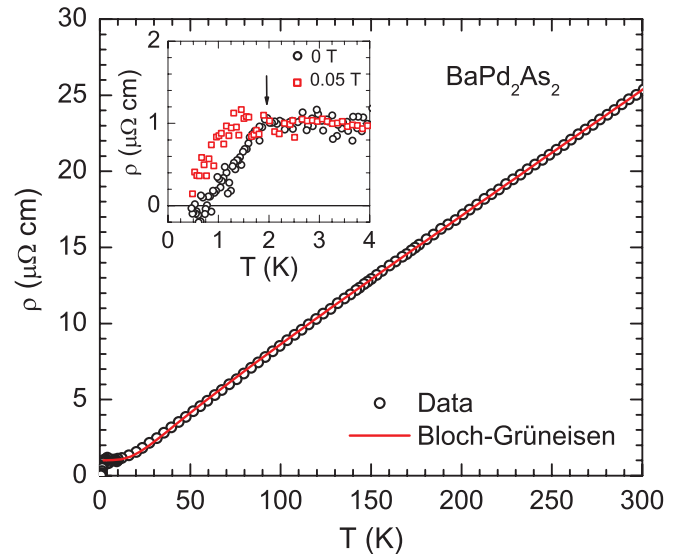


FIG. 16. (Color online) In-plane electrical resistivity ρ of a BaPd_2As_2 crystal versus temperature T measured in zero magnetic field H . The red curve is a fit by the Bloch-Grüneisen model. Inset: Expanded plot of the low- T $\rho(T)$ data showing the onset of superconductivity at $T \lesssim 2.0 \text{ K}$ measured at $H = 0$ and 0.05 T applied along the c axis. We infer that this superconductivity is filamentary and not bulk.

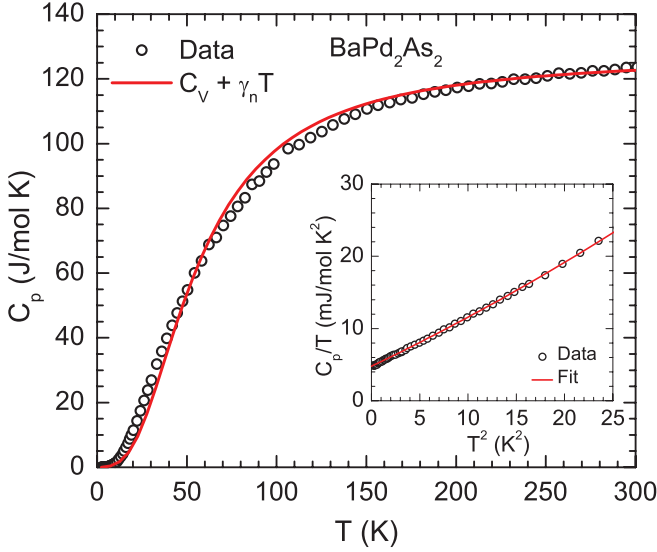


FIG. 17. (Color online) Heat capacity C_p of a BaPd_2As_2 single crystal versus temperature T for $2.4 \text{ K} \leq T \leq 300 \text{ K}$ measured in zero magnetic field. The red solid curve is the fitted sum of the contributions from the Debye lattice heat capacity $C_{V \text{ Debye}}(T)$ and predetermined electronic heat capacity $\gamma_n T$ according to Eq. (5a). Inset: C_p/T versus T^2 for $0.45 \text{ K} \leq T \leq 5 \text{ K}$. The red curve is a fit of the data by Eq. (3) for $0.45 \text{ K} \leq T \leq 5 \text{ K}$.

using Eq. (2d) is $\mathcal{R} = 9.34 \mu\Omega \text{ cm}$. The fit parameters are summarized in Table III.

The expanded low- T plot of $\rho(T)$ in the inset of Fig. 16 reveals an onset of superconductivity at $T_{\text{c onset}} \approx 2.0 \text{ K}$ for $H = 0$ with zero resistance at about 0.6 K . However, the transition width is very large compared to those of CaPd_2As_2 and SrPd_2As_2 , and the heat capacity measurements in the following section show no evidence for superconductivity above 0.45 K . An applied field of 0.05 T decreases $T_{\text{c onset}}$ by $\approx 0.8 \text{ K}$, as shown.

B. Heat capacity

The $C_p(T)$ data for BaPd_2As_2 are shown in Fig. 17. Like the other two compounds, the $C_p(T = 300 \text{ K}) = 124 \text{ J/mol K}$ is close to the expected high- T classical Dulong-Petit value. An expanded low- T plot of C_p/T versus T^2 is shown in the inset of Fig. 17. A fit of the data with $0.45 \text{ K} \leq T \leq 5 \text{ K}$ by Eq. (3) yields $\gamma_n = 4.79(2) \text{ mJ/mol K}^2$, $\beta = 0.638(5) \text{ mJ/mol K}^4$, and $\delta = 4.0(3) \mu\text{J/mol K}^6$, as shown by the red curve in the inset. A $\mathcal{D}_C(E_F) = 2.03(1) \text{ states/(eV f.u.)}$ for both spin directions is estimated from γ_n using Eq. (6). The value $\Theta_D = 248(1) \text{ K}$ is obtained from β using Eq. (4).

A value $\Theta_D = 227(2) \text{ K}$ is obtained by fitting the $C_p(T)$ data by Eqs. (5) over the entire T range ($2\text{--}300 \text{ K}$), as shown by the red curve in Fig. 17. Here again we used the analytic Padé approximant function⁵⁴ for $C_{V \text{ Debye}}(T)$ and set γ_n to the fixed value obtained above from the fit to the low- T $C_p(T)$ data. The normal-state parameters obtained from these fits are summarized in Table IV.

In contrast to the observation of the onset of superconductivity in the $\rho(T)$ data at $\approx 2.0 \text{ K}$ in the inset of Fig. 16, no corresponding feature is observed in the bulk $C_p(T)$ data

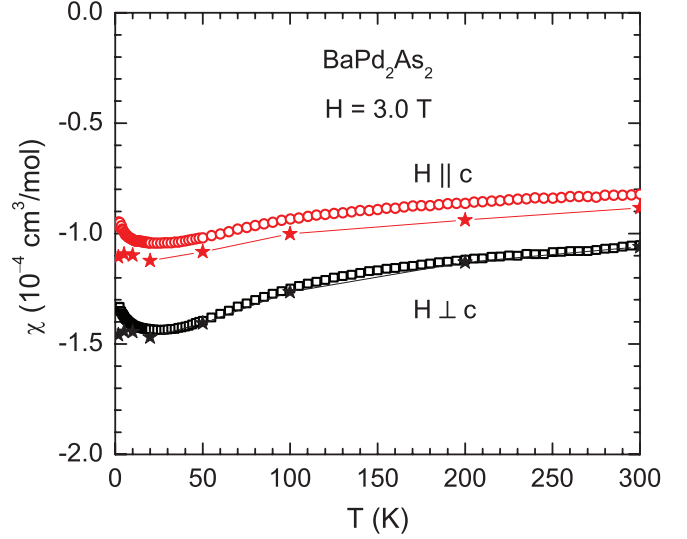


FIG. 18. (Color online) Zero-field-cooled magnetic susceptibility χ of a BaPd_2As_2 single crystal as a function of temperature T in the temperature range $1.8\text{--}300 \text{ K}$ measured in a magnetic field $H = 3.0 \text{ T}$ applied along the c axis (χ_c , $H \parallel c$) and in the ab plane (χ_{ab} , $H \perp c$). The filled stars are the intrinsic χ obtained in the Appendix from fitting $M(H)$ isotherm data by Eq. (A1). The lines joining the stars are guides to the eye.

above 0.45 K in the inset of Fig. 17, which indicates that there is no bulk superconductivity in BaPd_2As_2 and hence the superconductivity detected by the $\rho(T)$ measurements is filamentary in nature.

C. Magnetization and magnetic susceptibility

The anisotropic $\chi(T) \equiv M(T)/H$ data of a BaPd_2As_2 single crystal in $H = 3.0 \text{ T}$ are shown in Fig. 18. The χ is diamagnetic over the whole T range and exhibits a weak T dependence. We find that $\chi_c > \chi_{ab}$, which has the same sign of the χ anisotropy as in CaPd_2As_2 but is opposite to that of SrPd_2As_2 . One must keep in mind in making these comparisons that the crystal structure of BaPd_2As_2 is different from that of CaPd_2As_2 and SrPd_2As_2 . The intrinsic anisotropic susceptibilities obtained from the slopes of high-field linear fits to the $M(H)$ isotherms in the Appendix are shown by solid stars in Fig. 18. These data are in rather good agreement with the $\chi(T) \equiv M(T)/H$ data in Fig. 18 above 25 K , and indicate that the low- T upturns below 25 K are due to a small amount of paramagnetic impurities.

The different contributions to the intrinsic χ of BaPd_2As_2 were estimated following the same approach as for the Ca and Sr members above. The powder and temperature average of the intrinsic χ obtained from the analyses of the $M(H)$ isotherms from 1.8 to 300 K in the Appendix is $\langle \chi \rangle = -1.24 \times 10^{-4} \text{ cm}^3/\text{mol}$. We also obtain $\chi_{\text{core}} = -2.16 \times 10^{-4} \text{ cm}^3/\text{mol}$, $\chi_P = 6.6 \times 10^{-5} \text{ cm}^3/\text{mol}$ assuming $\mathcal{D}_{\text{band}}(E_F) = \mathcal{D}_C(E_F)$, and $\chi_L = -2.2 \times 10^{-5} \text{ cm}^3/\text{mol}$ [using $m_{\text{band}}^* = m_e$ in Eq. (50)]. A value $\langle \chi_{VV} \rangle = 4.8 \times 10^{-5} \text{ cm}^3/\text{mol}$ is then obtained using Eq. (48). These contributions are summarized in Table VI.

VIII. SUMMARY AND CONCLUSIONS

The crystallographic, electronic transport, thermal, magnetic and superconducting properties of APd_2As_2 ($A = \text{Ca}, \text{Sr}, \text{Ba}$) single crystals were investigated. The magnetic measurements in the normal state reveal anisotropic diamagnetism with $\chi_c > \chi_{ab}$ for CaPd_2As_2 and BaPd_2As_2 , and $\chi_{ab} > \chi_c$ for SrPd_2As_2 . The $\chi(T)$, $\rho(T)$, and $C_p(T)$ data indicate sp -band-like metallic behavior of all three compounds and provide conclusive evidence for bulk superconductivity in CaPd_2As_2 and SrPd_2As_2 but only filamentary superconductivity in BaPd_2As_2 which has a different crystal structure. The superconducting transition temperatures as estimated from the zero-field $C_p(T)$ data are $T_c = 1.27(3)$ K for CaPd_2As_2 and $T_c = 0.92(5)$ K for SrPd_2As_2 . The heat capacity jump at T_c , $\Delta C_e(T_c)$, of CaPd_2As_2 in $H = 0$ is extremely sharp, which allows unambiguous analysis of the derived electronic contribution $C_e(T)$ in the superconducting state. The $\Delta C_e(T_c)/\gamma_n T_c = 1.14(3)$ is significantly smaller than the BCS prediction of 1.43. We analyzed the $C_e(T)$ data in the superconducting state using the α -model,^{46,63} where $\alpha = \Delta(0)/k_B T_c$. A good fit to the data was obtained using $\alpha = 1.58$, which is significantly smaller than the BCS value of 1.764 which we surmise is due to anisotropy in the superconducting s -wave gap. The thermodynamic critical field $H_c(T)$ is also in agreement with the α -model prediction using the same value of α .

While the $\rho(T)$ data of CaPd_2As_2 exhibit a T_c consistent with that obtained from the $C_p(T)$ data, the $\rho(T)$ data of SrPd_2As_2 exhibit a higher T_c evidently due to filamentary nonbulk superconductivity. Our analysis of the normal and superconducting states $\rho(T, H)$ and $C_p(T, H)$ data of these two compounds and estimated superconducting parameters indicate type-II superconductivity with small thermodynamic critical fields and upper critical fields that are much smaller than those of the doped FeAs-based superconductors.

Note added. Recently, an electronic structure study of $(\text{Ca}, \text{Sr}, \text{Ba})\text{Pd}_2\text{As}_2$ appeared which largely substantiates our analyses of our experimental data for these compounds and offers additional perspectives.⁸⁰

ACKNOWLEDGMENTS

This research was supported by the U.S. Department of Energy, Office of Basic Energy Sciences, Division of Materials Sciences and Engineering. Ames Laboratory is operated for the U.S. Department of Energy by Iowa State University under Contract No. DE-AC02-07CH11358.

APPENDIX: PRESENTATION AND ANALYSIS OF $M(H)$ ISOTHERMS

1. CaPd_2As_2

The $M(H)$ isotherms for a CaPd_2As_2 crystal measured at eight temperatures between 1.8 and 300 K for H applied both along the c axis (M_c , $H \parallel c$) and in the ab plane (M_{ab} , $H \perp c$) are shown in Fig. 19. Consistent with the χ , the M is diamagnetic (negative) and exhibits weak anisotropy with $M_c(H) > M_{ab}(H)$. For $T \geq 50$ K, the $M(H)$ curves are almost linear in H , however, at low T a slight nonlinearity is observed that can be attributed to the presence of a small

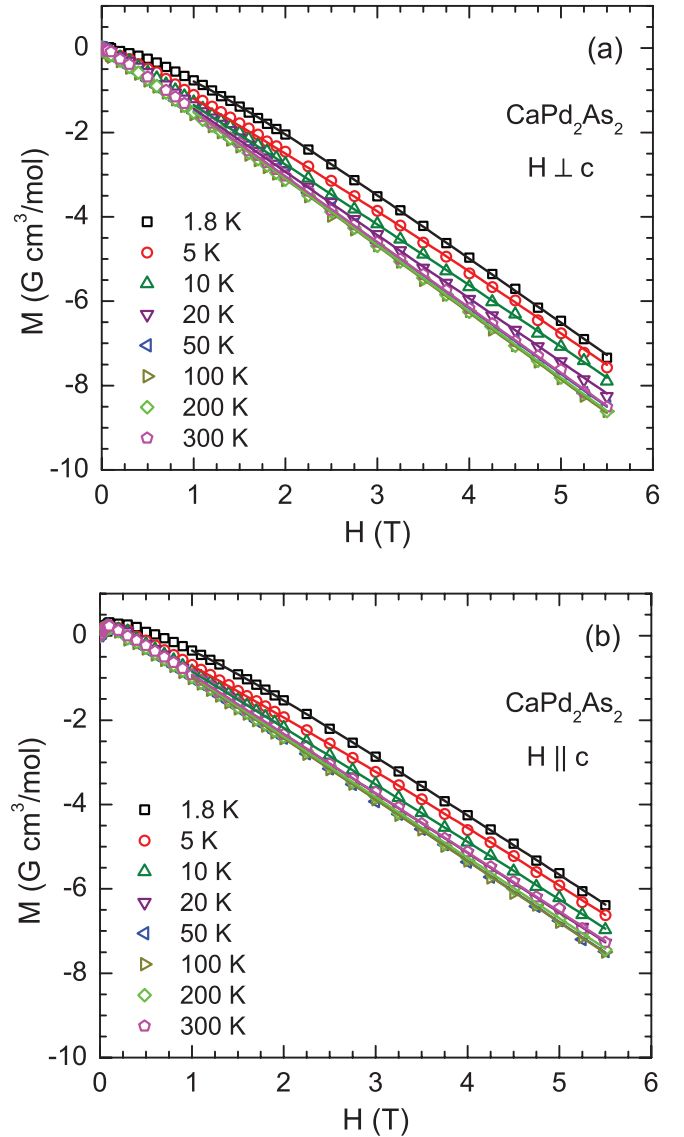


FIG. 19. (Color online) Isothermal magnetization M of CaPd_2As_2 versus applied magnetic field H at different temperatures, as listed, for magnetic fields applied (a) in the ab plane ($H \perp c$) and (b) along the c axis ($H \parallel c$). The solid curves are fits of the $M(H)$ data by Eqs. (A2) for $1.0 \leq H \leq 5.5$ T.

amount of saturable paramagnetic (PM) impurities. Further, the presence of trace amount of ferromagnetic (FM) impurities is also inferred from the $M(H)$ curves.

We estimated the FM impurity contribution by fitting the $M(H)$ data for $T \geq 50$ K and $H \geq 2$ T by

$$M(H) = M_s + \chi H, \quad (\text{A1})$$

where M_s is the FM impurity saturation magnetization. For $T \geq 50$ K the M_s is found to be almost T independent and anisotropic with values for $H \parallel c$ and $H \perp c$ listed in Table VIII. The M_s value of $0.48 \text{ G cm}^3/\text{mol}$ for $H \parallel c$ is equivalent to the saturation magnetization of 39 molar ppm of Fe metal impurities suggesting that only trace amounts of FM impurities are present in the crystal. However, due to the small magnitude of the diamagnetic χ even trace amounts of FM impurities are observable in χ and M measurements.

TABLE VIII. Parameters obtained from fitting $M(H)$ isotherms of APd_2As_2 ($A = \text{Ba}, \text{Ca}, \text{Sr}$) at 1.8 K by Eqs. (A1) and (A2), where $\theta_{\text{imp}} \equiv 0$ and $S_{\text{imp}} \equiv 2$. Here, M_s is the saturation magnetization of ferromagnetic impurities, χ is the intrinsic susceptibility, and f_{imp} is the molar fraction of the paramagnetic impurities.

Compound	Field direction	M_s ($\frac{\text{G cm}^3}{\text{mol}}$)	χ ($10^{-5} \frac{\text{cm}^3}{\text{mol}}$)	f_{imp} (10^{-4})
CaPd_2As_2	$H \perp c$	0.06(7)	-15.38(5)	1.01(2)
	$H \parallel c$	0.48(3)	-14.20(3)	0.86(1)
SrPd_2As_2	$H \perp c$	0.002(4)	-2.60(2)	
	$H \parallel c$	0.02(1)	-5.91(2)	
BaPd_2As_2	$H \perp c$	0.18(3)	-14.59(4)	
	$H \parallel c$	0.20(4)	-11.07(3)	

Once the FM impurity contributions M_s to the magnetizations were determined, we analyzed the low- T $M(H)$

data for both field directions by

$$M(T, H) = M_s + \chi H + f_{\text{imp}} M_{\text{Simp}} B_{\text{Simp}}(x). \quad (\text{A2a})$$

Here, χ is the intrinsic susceptibility of the compound, f_{imp} is the molar fraction of PM impurities, $M_{\text{Simp}} = N_A g_{\text{imp}} \mu_B S_{\text{imp}}$ is the PM impurity saturation magnetization, N_A is Avogadro's number, μ_B is the Bohr magneton, and g_{imp} and S_{imp} are the spectroscopic splitting factor (g factor) and the spin of the impurities, respectively. Our unconventional definition of the Brillouin function B_{Simp} is⁸¹

$$B_{\text{Simp}}(x) = \frac{1}{2S_{\text{imp}}} \left\{ (2S_{\text{imp}} + 1) \coth \left[(2S_{\text{imp}} + 1) \frac{x}{2} \right] - \coth \left(\frac{x}{2} \right) \right\}, \quad (\text{A2b})$$

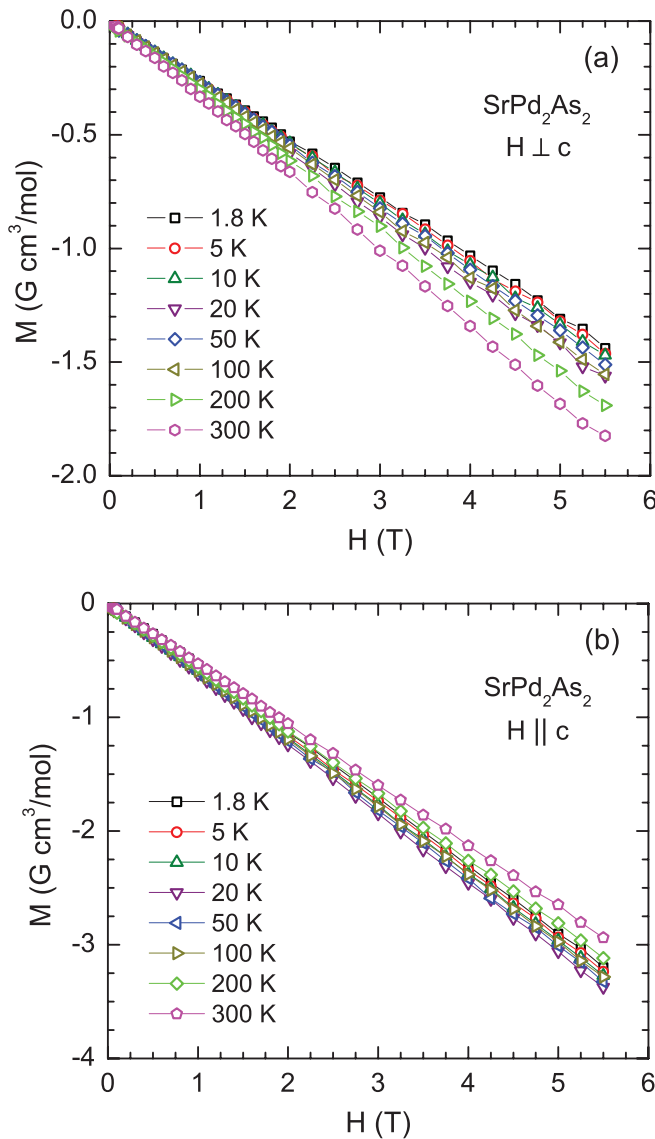


FIG. 20. (Color online) Isothermal magnetization M of SrPd_2As_2 versus magnetic field H at different temperatures as in Fig. 19.

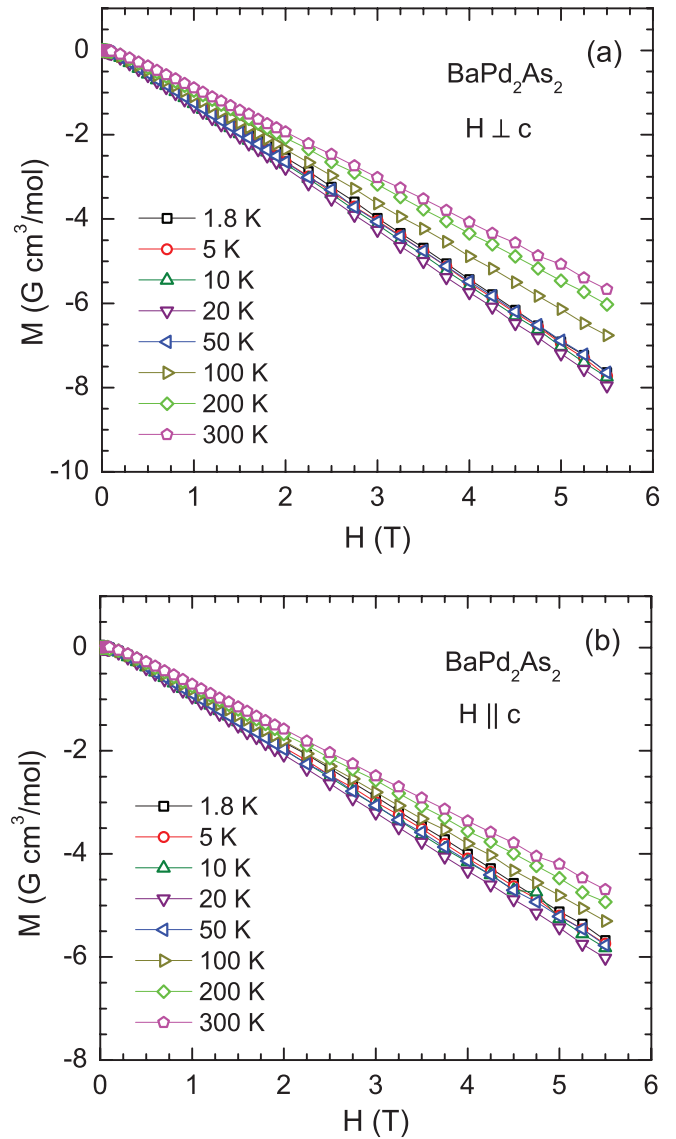


FIG. 21. (Color online) Isothermal magnetization $M(H)$ of BaPd_2As_2 versus magnetic field measured at different temperatures as in Fig. 19.

where

$$x \equiv \frac{g_{\text{imp}} \mu_B H}{k_B (T - \theta_{\text{imp}})}. \quad (\text{A2c})$$

A Weiss temperature θ_{imp} is included in the argument of $B_{S_{\text{imp}}}(x)$ to take into account for interactions between the paramagnetic impurities in an average mean-field way.

While fitting the $M(H)$ data the impurity g factor was set to $g_{\text{imp}} = 2$ and the M_s values for $H \perp c$ and $H \parallel c$ were set to the values listed in Table VIII. The $M(H)$ data for both H directions were fitted for magnetic fields in the range $1.0 \leq H \leq 5.5$ T. The S_{imp} values for both H directions were found to be $S_{\text{imp}} = 2.0(2)$; therefore, in the final fits we set $S_{\text{imp}} = 2$. The θ_{imp} values for both field directions were found to be close to zero and therefore in the final fits we set $\theta_{\text{imp}} \equiv 0$. The solid curves in Fig. 19 show the final fits of the $M(H)$ data by Eqs. (A2). The parameters obtained from the fits of the $M(H)$ isotherms at $T = 1.8$ K are listed in Table VIII. The intrinsic χ values obtained from the fits of the $M(H)$ data at different temperatures are shown by stars in Fig. 8. The T dependence of the intrinsic χ values clearly indicates that the low- T upturns in the measured $\chi(T) \equiv M(T)/H$ data are extrinsic.

2. SrPd₂As₂

The isothermal $M(H)$ data for a SrPd₂As₂ crystal at different T are shown in Fig. 20. Similar to the $\chi(T) \equiv$

$M(T)/H$ data in Fig. 14, the $M(H)$ data exhibit anisotropic diamagnetic behavior with $M_{ab}(H) > M_c(H)$. In order to obtain the contributions from the FM impurities, the $M(H)$ data for $H \geq 2$ T at $T \geq 1.8$ K were fitted by Eq. (A1) which gave the average M_s values of 0.002(4) for $H \perp c$ and 0.02(1) for $H \parallel c$. The fitting parameters for both $H \parallel c$ and $H \perp c$ for $T = 1.8$ K are listed in Table VIII. The intrinsic susceptibilities obtained from the analysis of $M(H)$ data by Eq. (A1) are shown by stars in Fig. 14. The paramagnetic impurity concentration is zero within our resolution since no curvature in the $M(H)$ curves on cooling to low T in addition to that due to the FM impurities was detected.

3. BaPd₂As₂

The $M(H)$ isotherms for a BaPd₂As₂ crystal at different T are shown in Fig. 21. The $M(H)$ curves exhibit weakly anisotropic diamagnetic behavior with $M_c(H) > M_{ab}(H)$. The intrinsic χ was obtained by fitting the $M(H)$ isotherms at each T by Eq. (A1) for $H \geq 2$ T which yielded temperature-averaged (for $T \geq 50$ K) FM saturation values $M_s^{ab} = 0.18(3)$ G cm³/mol and $M_s^c = 0.20(4)$ G cm³/mol which are equivalent to the magnetization contributions from 12 and 16 molar ppm of Fe metal impurities, respectively. As in the Sr compound, the paramagnetic impurity concentration is zero within our resolution since no curvature in the $M(H)$ curves on cooling to low T in addition to that due to the FM impurities was detected.

*vanand@ameslab.gov

†johnston@ameslab.gov

¹M. Rotter, M. Tegel, and D. Johrendt, *Phys. Rev. Lett.* **101**, 107006 (2008).

²G. F. Chen, Z. Li, G. Li, W.-Z. Hu, J. Dong, J. Zhou, X.-D. Zhang, P. Zheng, N.-L. Wang, and J.-L. Luo, *Chin. Phys. Lett.* **25**, 3403 (2008).

³K. Sasmal, B. Lv, B. Lorenz, A. M. Guloy, F. Chen, Y.-Y. Xue, and C. W. Chu, *Phys. Rev. Lett.* **101**, 107007 (2008).

⁴G. Wu, H. Chen, T. Wu, Y. L. Xie, Y. J. Yan, R. H. Liu, X. F. Wang, J. J. Ying, and X. H. Chen, *J. Phys.: Condens. Matter* **20**, 422201 (2008).

⁵H. S. Jeevan, Z. Hossain, D. Kasinathan, H. Rosner, C. Geibel, and P. Gegenwart, *Phys. Rev. B* **78**, 092406 (2008).

⁶A. S. Sefat, R. Jin, M. A. McGuire, B. C. Sales, D. J. Singh, and D. Mandrus, *Phys. Rev. Lett.* **101**, 117004 (2008).

⁷M. S. Torikachvili, S. L. Bud'ko, N. Ni, and P. C. Canfield, *Phys. Rev. Lett.* **101**, 057006 (2008).

⁸K. Ishida, Y. Nakai, and H. Hosono, *J. Phys. Soc. Jpn.* **78**, 062001 (2009).

⁹P. L. Alireza, Y. T. C. Ko, J. Gillett, C. M. Petrone, J. M. Cole, G. G. Lonzarich, and S. E. Sebastian, *J. Phys.: Condens. Matter* **21**, 012208 (2009).

¹⁰X. F. Wang, T. Wu, G. Wu, H. Chen, Y. L. Xie, J. J. Ying, Y. J. Yan, R. H. Liu, and X. H. Chen, *Phys. Rev. Lett.* **102**, 117005 (2009).

¹¹D. C. Johnston, *Adv. Phys.* **59**, 803 (2010).

¹²P. C. Canfield and S. L. Bud'ko, *Annu. Rev. Condens. Matter Phys.* **1**, 27 (2010).

¹³D. Mandrus, A. S. Sefat, M. A. McGuire, and B. C. Sales, *Chem. Mater.* **22**, 715 (2010).

¹⁴J. Paglione and R. L. Greene, *Nature Phys.* **6**, 645 (2010).

¹⁵P. Dai, J. Hu, and E. Dagotto, *Nature Phys.* **8**, 709 (2012).

¹⁶D. C. Johnston, in *Handbook of Magnetic Materials*, edited by K. H. J. Buschow (Elsevier, Amsterdam, 1997), Vol. 10, Chap. 1, pp. 1–237.

¹⁷A. Damascelli, Z. Hussain, and Z.-X. Shen, *Rev. Mod. Phys.* **75**, 473 (2003).

¹⁸P. A. Lee, N. Nagaosa, and X.-G. Wen, *Rev. Mod. Phys.* **78**, 17 (2006).

¹⁹P. C. Canfield, S. L. Bud'ko, N. Ni, J. Q. Yan, and A. Kracher, *Phys. Rev. B* **80**, 060501(R) (2009).

²⁰D. Kasinathan, A. Ormeci, K. Koch, U. Burkhardt, W. Schnelle, A. Leithe-Jasper, and H. Rosner, *New J. Phys.* **11**, 025023 (2009).

²¹C. Wang, Y. K. Li, Z. W. Zhu, S. Jiang, X. Lin, Y. K. Luo, S. Chi, L. J. Li, Z. Ren, M. He, H. Chen, Y. T. Wang, Q. Tao, G. H. Cao, and Z. A. Xu, *Phys. Rev. B* **79**, 054521 (2009).

²²L. J. Li, Q. B. Wang, Y. K. Luo, H. Chen, Q. Tao, Y. K. Li, X. Lin, M. He, Z. W. Zhu, G. H. Cao, and Z. A. Xu, *New J. Phys.* **11**, 025008 (2009).

²³A. S. Sefat, D. J. Singh, L. H. VanBebber, Y. Mozharivskyj, M. A. McGuire, R. Jin, B. C. Sales, V. Keppens, and D. Mandrus, *Phys. Rev. B* **79**, 224524 (2009).

²⁴K. Marty, A. D. Christianson, C. H. Wang, M. Matsuda, H. Cao, L. H. VanBebber, J. L. Zarestky, D. J. Singh, A. S. Sefat, and M. D. Lumsden, *Phys. Rev. B* **83**, 060509(R) (2011).

²⁵Y. Liu, D. L. Sun, J. T. Park, and C. T. Lin, *Physica C (Amsterdam)* **470**, S513 (2010).

- ²⁶J. S. Kim, S. Khim, H. J. Kim, M. J. Eom, J. M. Law, R. K. Kremer, J. H. Shim, and K. H. Kim, *Phys. Rev. B* **82**, 024510 (2010).
- ²⁷N. Ni, A. Thaler, A. Kracher, J. Q. Yan, S. L. Bud'ko, and P. C. Canfield, *Phys. Rev. B* **80**, 024511 (2009).
- ²⁸F. Han, X. Zhu, P. Cheng, G. Mu, Y. Jia, L. Fang, Y. Wang, H. Luo, B. Zeng, B. Shen, L. Shan, C. Ren, and H.-H. Wen, *Phys. Rev. B* **80**, 024506 (2009).
- ²⁹A. Thaler, N. Ni, A. Kracher, J. Q. Yan, S. L. Bud'ko, and P. C. Canfield, *Phys. Rev. B* **82**, 014534 (2010).
- ³⁰R. S. Dhaka, C. Liu, R. M. Fernandes, R. Jiang, C. P. Strehlow, T. Kondo, A. Thaler, J. Schmalian, S. L. Bud'ko, P. C. Canfield, and A. Kaminski, *Phys. Rev. Lett.* **107**, 267002 (2011).
- ³¹H. Wadati, I. Elfimov, and G. A. Sawatzky, *Phys. Rev. Lett.* **105**, 157004 (2010).
- ³²T. Berlijn, C.-H. Lin, W. Garber, and W. Ku, *Phys. Rev. Lett.* **108**, 207003 (2012).
- ³³C. Liu, T. Kondo, R. M. Fernandes, A. D. Palczewski, E. D. Mun, N. Ni, A. N. Thaler, A. Bostwick, E. Rotenberg, J. Schmalian, S. L. Bud'ko, P. C. Canfield, and A. Kaminski, *Nature Phys.* **6**, 419 (2010).
- ³⁴C. Liu, A. D. Palczewski, R. S. Dhaka, T. Kondo, R. M. Fernandes, E. D. Mun, H. Hodovanets, A. N. Thaler, J. Schmalian, S. L. Bud'ko, P. C. Canfield, and A. Kaminski, *Phys. Rev. B* **84**, 020509(R) (2011).
- ³⁵M. Neupane, P. Richard, Y.-M. Xu, K. Nakayama, T. Sato, T. Takahashi, A. V. Federov, G. Xu, X. Dai, Z. Fang, Z. Wang, G.-F. Chen, N.-L. Wang, H.-H. Wen, and H. Ding, *Phys. Rev. B* **83**, 094522 (2011).
- ³⁶E. M. Bittar, C. Adriano, T. M. Garitezi, P. F. S. Rosa, L. Mendonca-Ferreira, F. Garcia, G. de M. Azevedo, P. G. Pagliuso, and E. Granado, *Phys. Rev. Lett.* **107**, 267402 (2011).
- ³⁷J. A. McLeod, A. Buling, R. J. Green, T. D. Boyko, N. A. Skorikov, E. Z. Kurmaev, M. Neumann, L. D. Finkelstein, N. Ni, A. Thaler, S. L. Bud'ko, P. C. Canfield, and A. Moewes, *J. Phys.: Condens. Matter* **24**, 215501 (2012).
- ³⁸G. Levy, R. Sutarto, D. Chevrier, T. Regier, R. Blyth, J. Geck, S. Wurmehl, L. Harnagea, H. Wadati, T. Mizokawa, I. S. Elfimov, A. Damascelli, and G. A. Sawatzky, *Phys. Rev. Lett.* **109**, 077001 (2012).
- ³⁹S. Ideta, T. Yoshida, I. Nishi, A. Fujimori, Y. Kotani, K. Ono, Y. Nakashima, S. Yamaichi, T. Sasagawa, M. Nakajima, K. Kihou, Y. Tomioka, C. H. Lee, A. Iyo, H. Eisaki, T. Ito, S. Uchida, and R. Arita, *Phys. Rev. Lett.* **110**, 107007 (2013).
- ⁴⁰V. K. Anand, P. K. Perera, A. Pandey, R. J. Goetsch, A. Kreyssig, and D. C. Johnston, *Phys. Rev. B* **85**, 214523 (2012).
- ⁴¹V. K. Anand and D. C. Johnston, *Phys. Rev. B* **86**, 214501 (2012).
- ⁴²D. J. Singh, *Phys. Rev. B* **79**, 153102 (2009).
- ⁴³A. Mewis, *Z. Naturforsch.* **39b**, 713 (1984).
- ⁴⁴W. K. Hofmann and W. Jeitschko, *Monatsh. Chem.* **116**, 569 (1985).
- ⁴⁵H. Fujii and A. Sato, *Phys. Rev. B* **79**, 224522 (2009).
- ⁴⁶D. C. Johnston, arXiv:1304.2275.
- ⁴⁷J. Rodríguez-Carvajal, *Physica B (Amsterdam)* **192**, 55 (1993); see also www.ill.eu/sites/fullprof/.
- ⁴⁸R. Prozorov, R. W. Giannetta, A. Carrington, and F. M. Araujo-Moreira, *Phys. Rev. B* **62**, 115 (2000).
- ⁴⁹R. Prozorov and R. W. Giannetta, *Supercond. Sci. Technol.* **19**, R41 (2006).
- ⁵⁰R. Prozorov, R. W. Giannetta, A. Carrington, P. Fournier, R. L. Greene, P. Guptasarma, D. G. Hinks, and A. R. Banks, *Appl. Phys. Lett.* **77**, 4202 (2000).
- ⁵¹W. N. Hardy, D. A. Bonn, D. C. Morgan, R. Liang, and K. Zhang, *Phys. Rev. Lett.* **70**, 3999 (1993).
- ⁵²B. Cordero, V. Gómez, A. E. Platero-Prats, M. Revés, J. Echeverría, E. Cremades, F. Barragán, and S. Alvarez, *Dalton Trans.* **2008**, 2832 (2008).
- ⁵³F. J. Blatt, *Physics of Electronic Conduction in Solids* (McGraw-Hill, New York, 1968).
- ⁵⁴R. J. Goetsch, V. K. Anand, A. Pandey, and D. C. Johnston, *Phys. Rev. B* **85**, 054517 (2012).
- ⁵⁵C. Kittel, *Introduction to Solid State Physics*, 8th ed. (Wiley, New York, 2005).
- ⁵⁶E. S. R. Gopal, *Specific Heats at Low Temperatures* (Plenum, New York, 1966).
- ⁵⁷G. Grimvall, *Phys. Scr.* **14**, 63 (1976).
- ⁵⁸W. L. McMillan, *Phys. Rev.* **167**, 331 (1968).
- ⁵⁹T. K. Kim, A. N. Yaresko, V. B. Zabolotnyy, A. A. Kordyuk, D. V. Evtushinsky, N. H. Sung, B. K. Cho, T. Samuely, P. Szabó, J. G. Rodrigo, J. T. Park, D. S. Inosov, P. Samuely, B. Büchner, and S. V. Borisenko, *Phys. Rev. B* **85**, 014520 (2012).
- ⁶⁰M. Tinkham, *Introduction to Superconductivity*, 2nd ed. (Dover, Mineola, NY, 1996).
- ⁶¹V. G. Kogan, C. Martin, and R. Prozorov, *Phys. Rev. B* **80**, 014507 (2009).
- ⁶²J. Bardeen, L. N. Cooper, and J. R. Schrieffer, *Phys. Rev.* **108**, 1175 (1957).
- ⁶³H. Padamsee, J. E. Neighbor, and C. A. Shiffman, *J. Low Temp. Phys.* **12**, 387 (1973).
- ⁶⁴J. P. Carbotte, *Rev. Mod. Phys.* **62**, 1027 (1990).
- ⁶⁵P. G. de Gennes, *Superconductivity of Metals and Alloys* (Benjamin, New York, 1966).
- ⁶⁶E. Helfand and N. R. Werthamer, *Phys. Rev.* **147**, 288 (1966).
- ⁶⁷N. R. Werthamer, E. Helfand, and P. C. Hohenberg, *Phys. Rev.* **147**, 295 (1966).
- ⁶⁸A. M. Clogston, *Phys. Rev. Lett.* **9**, 266 (1962).
- ⁶⁹B. S. Chandrasekhar, *Appl. Phys. Lett.* **1**, 7 (1962).
- ⁷⁰K. Maki, *Phys. Rev.* **148**, 362 (1966).
- ⁷¹T. P. Orlando, E. J. McNiff Jr., S. Foner, and M. R. Beasley, *Phys. Rev. B* **19**, 4545 (1979).
- ⁷²S. Otake, M. Momouchi, and N. Matsuno, *J. Phys. Soc. Jpn.* **49**, 1824 (1980).
- ⁷³J. Heremans, C. H. Olk, and D. T. Morelli, *Phys. Rev. B* **49**, 15122 (1994).
- ⁷⁴L. B. Mendelsohn, F. Biggs, and J. B. Mann, *Phys. Rev. A* **2**, 1130 (1970).
- ⁷⁵N. W. Ashcroft and N. D. Mermin, *Solid State Physics* (Brooks Cole, Belmont, CA, 1976).
- ⁷⁶S. R. Elliott, *The Physics and Chemistry of Solids* (Wiley, Chichester, 1998).
- ⁷⁷J. D. Fletcher, A. Carrington, O. J. Taylor, S. M. Kazakov, and J. Karpinski, *Phys. Rev. Lett.* **95**, 097005 (2005).
- ⁷⁸J. D. Fletcher, A. Carrington, P. Diener, P. Rodiere, J. P. Brison, R. Prozorov, T. Olheiser, and R. W. Giannetta, *Phys. Rev. Lett.* **98**, 057003 (2007).
- ⁷⁹H. Kim, M. A. Tanatar, Y. J. Song, Y. S. Kwon, and R. Prozorov, *Phys. Rev. B* **83**, 100502 (2011).
- ⁸⁰I. A. Nekrasov and M. V. Sadovskii, arXiv:1305.3979.
- ⁸¹D. C. Johnston, R. J. McQueeney, B. Lake, A. Honecker, M. E. Zhitomirsky, R. Nath, Y. Furukawa, V. P. Antropov, and Y. Singh, *Phys. Rev. B* **84**, 094445 (2011).